



Imaging the mantle transition zone beneath East Asia using teleseismic receiver functions: implications for thermal and compositional heterogeneities

Hyunsun Kang, Raymond M. Russo & YoungHee Kim

To cite this article: Hyunsun Kang, Raymond M. Russo & YoungHee Kim (05 Feb 2026): Imaging the mantle transition zone beneath East Asia using teleseismic receiver functions: implications for thermal and compositional heterogeneities, International Geology Review, DOI: [10.1080/00206814.2026.2624755](https://doi.org/10.1080/00206814.2026.2624755)

To link to this article: <https://doi.org/10.1080/00206814.2026.2624755>



© 2026 The Author(s). Published by Informa UK Limited, trading as Taylor & Francis Group.



[View supplementary material](#)



Published online: 05 Feb 2026.



[Submit your article to this journal](#)



[View related articles](#)



[View Crossmark data](#)

Imaging the mantle transition zone beneath East Asia using teleseismic receiver functions: implications for thermal and compositional heterogeneities

Hyunsun Kang^{a,b}, Raymond M. Russo^c and YoungHee Kim^{a,b}

^aResearch Center for Deep-Surface Coupling of Earth, Seoul National University, Seoul, Republic of Korea; ^bSchool of Earth and Environmental Sciences, Seoul National University, Seoul, Republic of Korea; ^cDepartment of Geological Sciences, University of Florida, Gainesville, FL, USA

ABSTRACT

The mantle transition zone (MTZ) plays a critical role in regulating material flux and mixing between the upper and lower mantle. Variations in MTZ structure are closely associated with mantle temperature and compositional heterogeneities, making it essential to constrain these variations to better understand mantle dynamics. To investigate the MTZ structure beneath East Asia, where the stagnant Pacific slab and intraplate volcanism provide a unique geodynamic setting, we examined over 40,000 *P*-to-*S* converted waves from 18 seismic networks in Korea, China, and Japan. Common conversion point (CCP) stacking revealed significant regional variations in MTZ discontinuities and heterogeneous lateral variations in converted wave amplitudes. The average depths of the 410-km (d410) and 660-km (d660) discontinuities were 416 ± 10 km and 668 ± 11 km, respectively, yielding a mean MTZ thickness of 252 ± 14 km with notable localized deviations. CCP-stacked profiles at 0.2 Hz and 0.5 Hz highlighted the structural complexities, revealing evidence for multi-layered MTZ boundaries. Converted wave amplitudes exhibited lateral variations on scales of 200 km and larger; however, these variations in amplitudes did not correlate with the variations in discontinuity depths. A pronounced depression of the d660 beneath the Korean Peninsula and northeastern China likely reflects the influence of the cold, stagnant, and near-horizontal Pacific slab. The accompanying d410 depression beneath the Korean Peninsula suggests compositional heterogeneity, possibly linked to water and carbon enrichment. Near-normal MTZ discontinuity structures beneath the Ulleung and Jeju intraplate volcanoes indicate limited influence from the stagnant Pacific slab, potentially due to a slab tear or a localized thermal anomaly near the base of the MTZ. Mantle upwelling through such a tear is likely hydrous rather than purely thermal, consistent with the near-normal d410. These results demonstrate that regional MTZ anomalies reflect interactions among mantle upwelling, slab-derived heterogeneities, and volatile-rich components.

ARTICLE HISTORY

Received 5 June 2025

Accepted 24 January 2026

KEYWORDS

East Asia; intraplate volcanism; mantle discontinuities; mantle transition zone; receiver function

1. Introduction

1.1. Mantle transition zone and its geodynamic significance

The mantle transition zone (MTZ), bounded by seismic discontinuities at depths of 410 km and 660 km (d410 and d660), plays a crucial role in mantle dynamics by regulating material and heat exchange between the upper and lower mantle (e.g. Bercovici and Karato 2003). These discontinuities are associated with mineral phase transitions, specifically, the transformation of olivine to wadsleyite at d410 (e.g. Katsura and Ito 1989) and the transition from ringwoodite to bridgmanite and ferropericlase at d660 (e.g. Ito and Takahashi 1989; Katsura *et al.* 2003). These phase transitions lead to density and viscosity contrasts

that can either impede or facilitate material flow across the MTZ. Consequently, they influence geodynamic processes such as the stagnation of subducted slabs, by hindering their descent into the lower mantle, and the ponding or deflection of mantle plumes rising from the deep mantle (e.g. Fukao *et al.* 2009).

1.2. Compositional and thermal controls on MTZ structure

The structure of the MTZ discontinuities provides crucial constraints on both thermal and compositional variations within the mantle. The phase transitions at depths of 410 km and 660 km exhibit opposite Clapeyron slopes – positive for d410 and

CONTACT YoungHee Kim  younghkim@snu.ac.kr  Research Center for Deep-Surface Coupling of Earth, Seoul, Seoul National University, 1 Gwanak-ro, Gwanak-gu, Seoul 08826, Republic of Korea

 Supplemental data for this article can be accessed online at <https://doi.org/10.1080/00206814.2026.2624755>

© 2026 The Author(s). Published by Informa UK Limited, trading as Taylor & Francis Group.

This is an Open Access article distributed under the terms of the Creative Commons Attribution-NonCommercial-NoDerivatives License (<http://creativecommons.org/licenses/by-nc-nd/4.0/>), which permits non-commercial re-use, distribution, and reproduction in any medium, provided the original work is properly cited, and is not altered, transformed, or built upon in any way. The terms on which this article has been published allow the posting of the Accepted Manuscript in a repository by the author(s) or with their consent.

negative for d660 – resulting in a thickened MTZ in colder regions and a thinned MTZ in hotter regions (Bina and Helffrich 1994). In addition to temperature, compositional heterogeneities, such as the presence of water and carbon derived from subducting slabs, can also affect the MTZ discontinuities. A series of experimental and computational studies suggest that water has a strong effect on the post-spinel transition (dissociation of ringwoodite to bridgmanite and ferropericlase), making it a plausible candidate for the depression of d660 (Litasov *et al.* 2005; Ghosh *et al.* 2013; Muir *et al.* 2021). Similarly, d410 shifts to shallower depths under wet conditions (Chen *et al.* 2002; Litasov *et al.* 2005; Frost and Dolejš 2007). However, under specific conditions, the transition may become more complex or be influenced by overlapping phase boundaries, which can obscure its seismic signature. For example, Schmerr and Garnero (2007) suggested that localized seismic reflectors near a depth of 410 km, which result from boundaries between hydrated and anhydrous wadsleyite, could produce the apparent deepening of d410. Layers of slow seismic velocity observed just above d410 (e.g. Liu *et al.* 2016; Tauzin *et al.* 2017; Han *et al.* 2021) have been associated with partial melting of the upper mantle induced by volatiles such as water (Bercovici and Karato 2003) and carbon (Kim and Lee 2025). The differential solubility of carbon in olivine and wadsleyite (Shcheka *et al.* 2006) may also increase the depth of d410. Collectively, these findings indicate that both water and carbon play key roles in controlling the depths and seismic characteristics of MTZ discontinuities.

In addition to potential variability in MTZ structure due to heterogeneous distributions of volatiles, the presence of recycled crustal material and variations in mantle mineralogy may also contribute to MTZ heterogeneity. Subducted oceanic crust, enriched in basalt, can modify the density and seismic velocity contrasts across the MTZ discontinuities (Bissig *et al.* 2022; Yu *et al.* 2023). Additionally, the phase transition from majoritic garnet to perovskite, which dominates at higher temperatures, may deepen or broaden d660 and contribute to regional MTZ thickening (Hirose 2002; Wang and Niu 2010; Jenkins *et al.* 2016; Wang and He 2020). Notably, in cold subduction zones, the transition of akimotoite ($MgSi$ -ilmenite) to bridgmanite has been suggested to depress d660 to about 750 km (Chanyshhev *et al.* 2022). These findings suggest that the MTZ structure provides a critical window into the thermal, chemical, and geodynamic processes of the mantle.

1.3. Stagnant Pacific slab and its role in East Asian mantle dynamics

One of the most prominent features of East Asian mantle dynamics is the stagnant segment of the subducted Pacific Plate that lies near-horizontally in the MTZ beneath Japan, Korea, and China (e.g. Fukao and Obayashi 2013). This stagnation plays a crucial role in modulating subduction-related processes, including slab dehydration, volatile recycling, and melt generation, all of which impact intraplate volcanism and regional tectonics (Liu *et al.* 2017; Zhao 2021). As the slab stagnates in the MTZ, it gradually releases water and other volatiles through mineral breakdown reactions, which are transported upward into the overlying mantle, lowering the solidus temperature of surrounding mantle materials, promoting partial melting and potentially feeding intraplate volcanism. Additionally, the residual slab material may mechanically influence mantle flow and stress distribution, thereby impacting regional tectonics. Therefore, constraining the spatial extent of the stagnant Pacific Plate and thermochemical characteristics of the MTZ is essential for understanding mantle convection patterns and the broader geodynamic framework of East Asia.

The study of the MTZ beneath the Korean Peninsula provides a unique opportunity to investigate subduction-related mantle dynamics at a continental margin that bridges the tectonic regimes of China and Japan. Characterizing the depth and thermochemical properties of the MTZ discontinuities is critical for assessing the role of the stagnant Pacific slab in driving intraplate volcanism along the eastern margin of the Eurasian Plate. In this study, we analyse teleseismic P -to- S converted waves to constrain the MTZ structure beneath East Asia and examine its connection to intraplate volcanism. We aim to clarify the thermal and compositional characteristics of the MTZ across East Asia and evaluate the role of stagnant slab-mantle interactions in generating surface manifestations of intraplate volcanism.

2. Geophysical and geochemical perspectives on MTZ structure and intraplate volcanism in East Asia

2.1. MTZ structure of East Asia

Previous studies have explored the MTZ structure beneath East Asia, particularly China and Japan, in some detail. High-resolution seismic data have provided valuable insights into slab stagnation and mantle heterogeneities. In Northeast China, seismic tomography studies image a stagnant Pacific slab in

the MTZ beneath a prominent slow-velocity anomaly situated below the Changbaishan volcanic region (known as Baekdu-san in Korean), which is attributed to slab dehydration and subsequent convective circulation of hydrous mantle material (e.g. Zhao et al. 2009, 2025). Studies further reveal that the d660 is significantly depressed (by approximately 20–30 km) beneath and around the Changbaishan/Baekdu-san (Ai et al. 2003; Li and Yuan 2003; Liu et al. 2015; Zhang et al. 2016; Sun et al. 2020, 2022). This depression has been attributed to slab stagnation and hydration of the MTZ, in turn triggering intraplate volcanism in the region (Liu et al. 2015; Tian et al. 2016; Sun et al. 2020).

High-density seismic networks in Japan have enabled detailed imaging of the MTZ and subducting Pacific and Philippine Sea slabs beneath the Japanese islands (Li et al. 2000; Niu et al. 2005; Tonegawa et al. 2005). Observations reveal a narrow uplift of the d410 and a broad depression of the d660 beneath southwestern Japan, consistent with Clapeyron slope predictions, induced by subduction of cold Pacific slab that lies flat above or across the d660, as observed in tomography models (Collier and Helffrich 1997; Castle and Creager 1998; Niu et al. 2005; Ramesh et al. 2005). In contrast, northeastern Japan exhibits relatively flat MTZ discontinuities, interpreted as reflecting the effects of MTZ hydration rather than high temperature, potentially linked to a wet plume originating from the lower mantle (Miyazaki and Nakajima 2025).

The recent expansion of broadband seismic networks in South Korea enables detailed investigation of MTZ structures that bridge the tectonic regimes of Northeast China and Japan. Prior studies suggest that the deflection of the d660 observed beneath southwestern Japan extends westward beneath the Korean Peninsula, indicating possible dynamic interaction between the stagnant Pacific Plate and the MTZ in this region (Lee et al. 2014; Sun et al. 2022). Ai et al. (2008) detected a locally shallow d660 beneath the northern Yellow Sea, which was interpreted as evidence of hot mantle upwelling, either from a small-scale convection triggered by slab penetration into the lower mantle or from a small upwelling plume. Lee et al. (2014) reported that a depressed d410 extended from the Korean Peninsula to Kyushu, along with a pronounced north-south variation in the depth of d660. The deeper d660 observed south of 36°N was attributed to a different slab subduction angle and heterogeneity in slab water content. More recently, Sun et al.

(2022) identified an ESE-WNW-elongated zone of significant MTZ thinning extending from central Honshu to the Korean Peninsula, which they interpret as a large-scale slab tear through which hot ascending material flows.

2.2. *Intraplate volcanism at Ulleung and Jeju Islands*

The Cenozoic intraplate volcanic systems on Ulleung and Jeju Islands, situated off the eastern and southern coasts of Korea, respectively, offer valuable insights into the mantle processes operating beneath the East Asian margin (Brenna et al. 2012; Chen et al. 2018). Geochemical analyses of Ulleung volcanic rocks show wide variations in isotopic and trace-element compositions, indicating the contribution of both depleted and enriched mantle components (Brenna et al. 2014; Chen et al. 2018). Such geochemical diversity suggests a heterogeneous mantle source potentially influenced by regional subduction processes and lithosphere–asthenosphere interactions (Kim et al. 2008; Choi 2021; Lee et al. 2021). Water and gas geochemistry of springs on the island indicates the presence of upper mantle-derived volatiles, providing evidence of ongoing degassing processes (Lee et al. 2025). Several geophysical studies also reveal slow-velocity anomalies extending to the MTZ (Simuté et al. 2016; Wei and Zhao 2020) and a relatively thin MTZ near the Ulleung Island (Sun et al. 2022), which are associated with mantle upwelling within the MTZ.

Cenozoic volcanism at Jeju Island has been a subject of debate, particularly regarding the role of stagnant Pacific slab in the MTZ. Seismic tomography of Jeju reveals slow-velocity anomalies extending to depths of 50–60 km (Song et al. 2018), although a regional-scale seismic velocity model shows slow-velocity anomalies reaching the bottom of the MTZ (Y.-W. Kim et al. 2021); their origin remains uncertain. Geochemical data at Jeju suggest contributions from recycled oceanic crust and sedimentary materials (Kim et al. 2019; Choi et al. 2024; Kim and Choi 2025), as well as possible contribution from the subcontinental lithospheric mantle affected by localized asthenospheric upwelling (D. Kim et al. 2021). Additional hypotheses include a mantle plume origin (Tatsumi et al. 2005), distant effects of subduction-related tectonics at the Kyushu subduction zone (Brenna et al. 2015), and decompression melting associated with lithospheric folding near collisional plate boundaries (Shin et al. 2012). These competing interpretations highlight the heterogeneity of mantle sources of magmatism at the two sites, indicating that further constraining variations in MTZ structure and thermochemical state in this area is highly desirable.

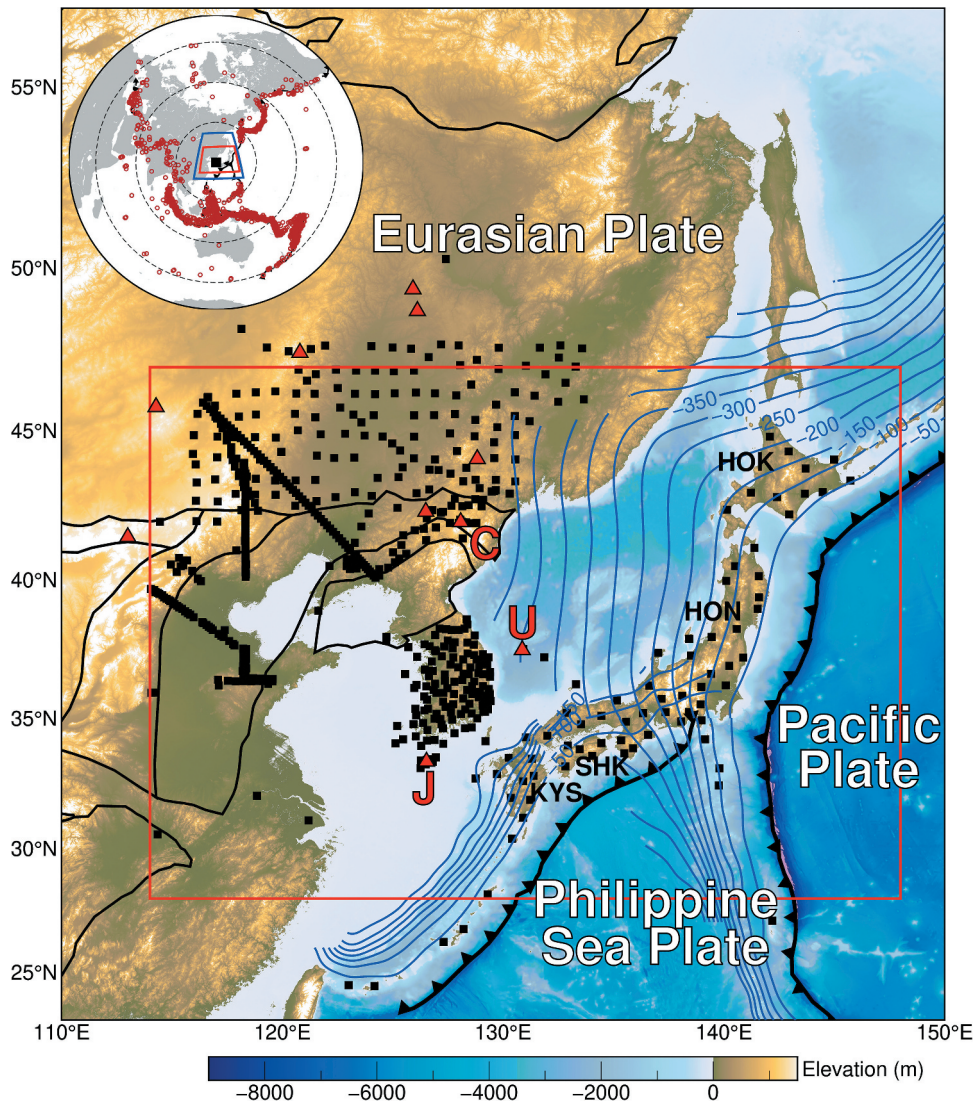


Figure 1. Topographic map (SRTM 15 arcsecond elevations) of East Asia. Seismic stations used in this study are shown as black squares. Blue lines are contours (interval 50 km) marking the top of the subducted Pacific and Philippine Sea plates (Slab2.0; Hayes *et al.* 2018). Black lines denote cratonic boundaries from the global tectonic dataset of Hasterok *et al.* (2022). Red triangles indicate the major Holocene intraplate volcanic fields of East Asia (J: Jeju Island, U: Ulleung Island, C: Changbaishan/Baekdu-san). The four main Japanese islands are labelled as HOK (hokkaido), HON (Honshu), SHK (shikoku), and KYS (Kyushu). The inset shows the locations of the teleseismic earthquakes (red circles) used when computing RFs. Dashed circles indicate epicentral distances of 30°, 60°, and 90° from the centre of the study area (black square). The area within the blue rectangle is displayed in a zoomed-in view. The focus area of this study is highlighted in the red rectangle both in the inset and the zoomed-in view.

3. Data and methods

3.1. Data

We collected seismic waveform data from 631 broadband stations operated by 18 seismic networks across East Asia (Figure 1). Recording durations for each station are listed in Table S1. The study area spans approximately 114°–148°E and 28°–47°N, covering the Korean Peninsula, Japan, and northeastern China. We selected earthquakes of magnitude >6.0 at epicentral distances of 30°–90°. We rotated three-component seismograms to a radial–

tangential–vertical (R-T-Z) coordinate system and selected waveforms whose average signal-to-noise ratio (SNR) for the vertical and radial components was >9. The SNR was defined as $20 \times \log_{10}(A_{\text{signal}}/A_{\text{noise}})$, where A_{signal} and A_{noise} are the standard deviations of normalized waveforms within 30 s signal and noise windows before and after the P-wave arrival times, respectively. The selected waveforms were then bandpass-filtered between 0.02 and 2 Hz and cut 30 s before and 300 s after the direct P-wave arrivals. For stations on the Korean Peninsula with known horizontal-component misorientations, the

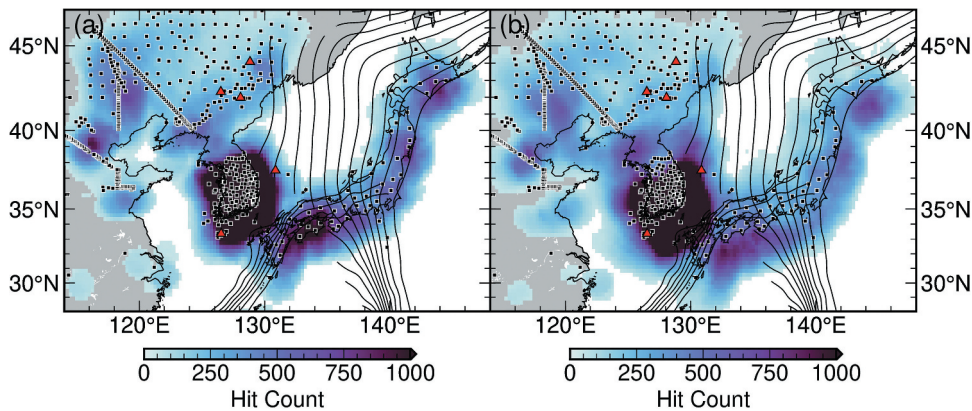


Figure 2. Hit counts at depths of 410 km (a) and 660 km (b) backprojected using the EARA2024 model. These counts indicate the total number of *P*-to-*S* piercing points within a 1° radius of each bin. Black squares: seismic stations. Black lines: contours (interval of 50 km) marking the top of the subducted Pacific and Philippine Sea plates (Slab2.0; Hayes *et al.* 2018). The other symbols are the same as those of Figure 1. The spatial distributions of the *P*-to-*S* piercing points at depths of 410 km and 660 km are shown in Figure S1.

orientations were corrected using the angles reported by Son *et al.* (2022).

Our dataset provides unprecedentedly dense coverage across South Korea, enabling robust imaging of the MTZ structure along the easternmost margin of the Asian craton. The spatial distribution is, however, irregular, with mainland China relatively under-sampled (Figure 2), primarily due to limited access to several Chinese networks. To assess the potential influence of this uneven coverage, in uncertainty from uneven data coverage in Northeastern China (below), we compare our results with recent studies that achieved broader coverage in mainland China (Sun *et al.* 2020; L. Liu *et al.* 2022).

3.2. Receiver function calculation

We used the *P*-to-*S* receiver function (RF) technique, which is particularly effective for detecting velocity discontinuities beneath seismic stations. The RF calculation involves deconvolution to isolate the impulse response of the Earth's structure by removing the source time function and instrumental response from the radial component of the seismogram (Ammon 1991). The R and T components were deconvolved by the Z component to obtain the corresponding RFs.

We used time-domain iterative deconvolution (Ligorría and Ammon 1999), in which the RF is constructed by iteratively summing Gaussian pulses, defined by the function $G(w) = e^{-\frac{w^2}{4a^2}}$, with the Gaussian filter width parameter (a) of 0.4 and 1 rad s^{-1} . We limited the number of iterations to 5000. These values correspond to filter gains of 0.1 at corner frequencies of 0.2 Hz and 0.5 Hz, respectively, allowing us to image the frequency-dependent sharpness of seismic discontinuities.

This filter was also applied to pre-filter the R- and Z-component seismograms. The R-component RFs were then normalized by the maximum amplitude of the Z-component RFs, obtained by self-deconvolution of the Z-component. This normalization preserves the true relative amplitude of the *P*-to-*S* converted phases with respect to the direct *P* arrivals, independent of the choice of Gaussian filter width.

After computing the RFs, we performed a four-step automated quality control procedure. RFs were rejected if they: (1) exhibited a negative trough at 0 s, (2) had high amplitudes in the R-component RFs ($0.4 \times$ the amplitude of the first *P*-wave arrival) after the first *P*-wave arrival, (3) showed strong resonance or ringing in their coda, or (4) had a higher amplitude in the T-component RF than in the R-component RF at initial *P*-wave arrival (0 s). A total of 43,283 RFs passed the quality criteria for $a = 0.4 \text{ rad s}^{-1}$, while 49,664 RFs passed for $a = 1 \text{ rad s}^{-1}$. The number of RFs at each station is listed in Table S1.

3.3. Common conversion point stacking

We applied common conversion point (CCP) stacking (Dueker and Sheehan 1997) to the RFs to suppress random noise and to constrain lateral variations in upper mantle discontinuities beneath the study region. In this analysis, RFs were ray-traced back to their theoretical *P*-to-*S* conversion points and migrated to depth. The study area was gridded into bins of $0.25^\circ \times 0.25^\circ$. For each bin, we used a circular cap with a 1° radius to gather RF amplitudes. These amplitudes were then averaged to represent the subsurface seismic structure within each bin. We calculated the arrival time differences between the direct *P* wave and the *P*-to-*S* converted phases (*Pds*) at upper mantle discontinuities (i.e. *Pds*–*P* time), and the

locations of their corresponding piercing points at 5 km depth intervals from 5 km to 800 km. These calculations were performed using 1-D global (IASP91; Kennett and Engdahl 1991), 3-D regional (FWEA18; Tao *et al.* 2018, EARA2024; Xi *et al.* 2024), and global (TX2019slab; Lu *et al.* 2019) seismic velocity models. Figure 2 shows hit count maps of P -to- S conversion points at 410 km and 660 km depths, backprojected using the EARA2024 model. Elevation corrections were applied to account for differences in station elevations. To avoid overestimating the Pds - P time – and thus the MTZ thickness (Lawrence and Shearer 2006) – we used depth- and distance-dependent ray parameters for the Pds phases, ensuring more accurate time-to-depth conversion in CCP stacking.

To account for the dependence of converted-phase amplitudes on incidence angle, we applied a ray-parameter-dependent amplitude correction to the stacked amplitude maps (Figure 6). Correction factors were derived from synthetic RFs computed using the reflectivity-based method (Kennett 1983; Randall 1994) with the IASP91 velocity model, in which the relative amplitudes of P410s and P660s were quantified as a function of ray parameter.

4. Results

4.1. Relief of MTZ discontinuities

Seismic observations reveal strong regional variations in the depths of the MTZ discontinuities (Figure 3).

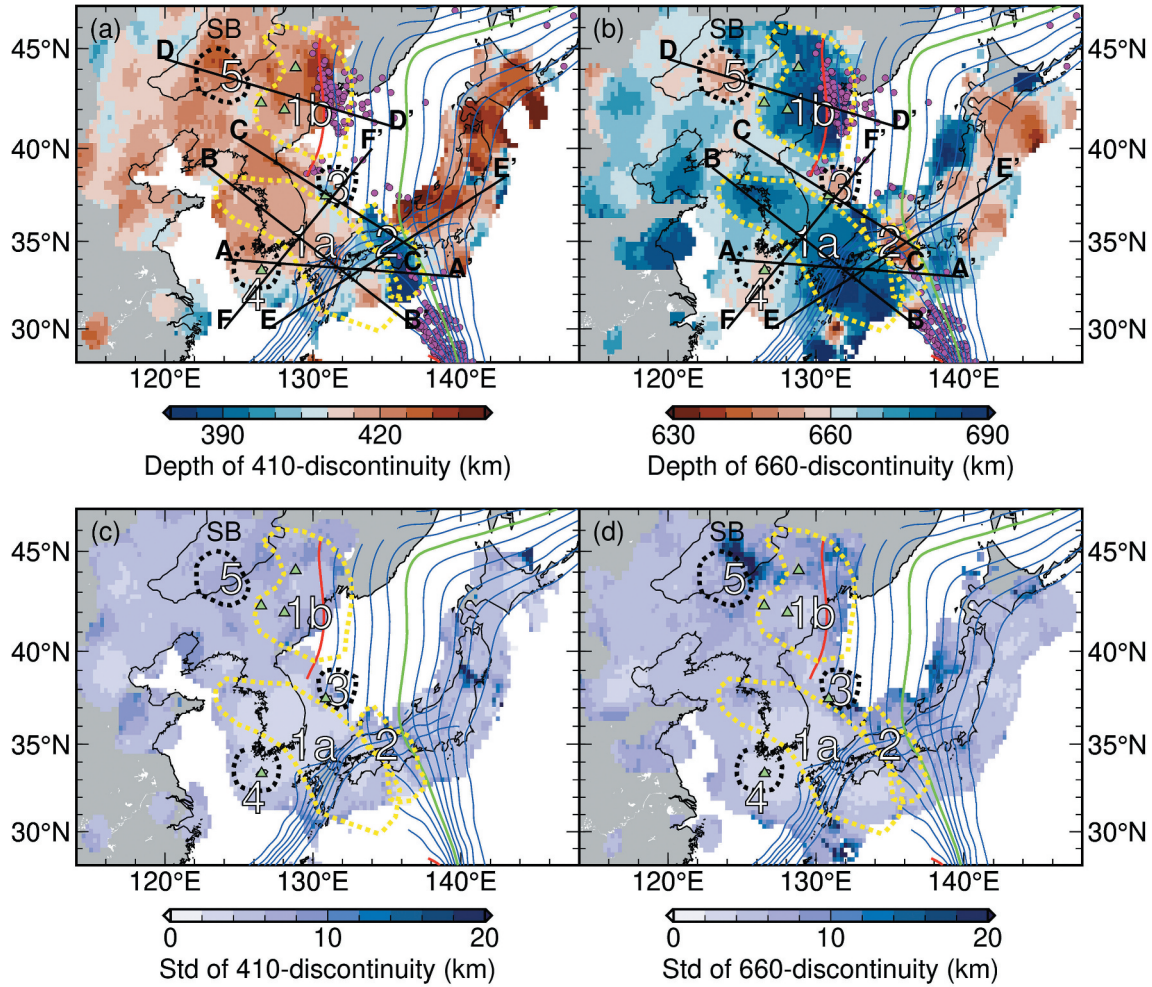


Figure 3. Depths of the 410-km discontinuity (a) and 660-km discontinuity (b) derived from CCP stacking of RFs using the 3-D EARA2024 model (Xi *et al.* 2024). Bootstrap uncertainties of the depths of the d410 (c) and d660 (d) are shown. Discontinuity depths are shown only in regions where the sampling hit count exceeded 50. Magenta circles show the hypocentre locations of earthquakes deeper than 500 km that occurred between 1964 and 2010 (International Seismological Centre 2024). Blue lines are contours of the top slab interface (Hayes *et al.* 2018); the 550-km contour for the Pacific slab is shown in red and the 300-km contour in green. Green triangles show locations of Holocene intraplate volcanic fields in East Asia. Black outlined area marks the location of the Songliao basin (SB). Black and yellow dotted lines refer to areas discussed in the text, keyed by large numbers. Black lines labelled A-A', etc., show the locations of cross sections (see Figure 4).

Specifically, the depth of the d410 interface ranges from 380 to 440 km, with an average of 416 ± 10 (1σ) km (Figure S2). The depth of the d660 interface ranges between 623 and 704 km, with a mean of 668 ± 11 (1σ) km. The depth distribution of d410 exhibits a negative skewness of -0.6 , indicating a left-skewed distribution towards shallower depths, while the d660 depths display a slight positive skewness of 0.2 , suggesting a weak right-skewness towards greater depths. These depth variations result in MTZ thicknesses ranging from 206 to 300 km, with an average of 252 ± 14 km (1σ), which is consistent with the global average of 250 km specified in the IASP91 model (Kennett and Engdahl 1991). To further investigate the structural complexity, we identified five subregions exhibiting distinct characteristics in the relief of the MTZ discontinuities.

4.1.1. Broad depressions of d660 and d410 discontinuities

The most prominent feature of the MTZ beneath the Korean Peninsula and northeastern China is a broad depression of the d660 discontinuity. This depression is especially pronounced in two areas, labelled Area 1a (678 ± 6 km) and Area 1b (680 ± 8 km) in Figure 3b. Area 1a, which we refer to hereafter as the Southern Stagnant Pacific Slab Anomaly (SSPSA), extends from southwestern Japan to the west-central Korean Peninsula (30° – 38.5° N, 124° – 136° E), while Area 1b, hereafter the Northern Stagnant Pacific Subduction Anomaly (NSPSA), is located beneath the east coast of the northeastern Korean Peninsula (39.5° – 46° N, 126° – 133° E). The NSPSA (Area 1b) includes clusters of deep-focus earthquakes (>500 km depth) and lies beneath several Cenozoic intraplate volcanic fields, including Changbaishan/Baekdu-san (marked as C in Figure 1). The depths to d410 for the two areas are 413 ± 8 km (SSPSA) and 422 ± 6 km (NSPSA). Although the average depression of the d410 across the SSPSA is small (3 ± 8 km), localized depressions reach 8 ± 3 km beneath the Korean Peninsula, indicating spatially heterogeneous behaviour of the 410-km interface. MTZ thicknesses exceeding the global average of 250 km suggest that the d660 depression is more substantial than that of the d410.

4.1.1.1. Southern Stagnant Pacific Slab Anomaly.

Our results reveal a pronounced depression of the d660 in the Southern Stagnant Pacific Slab Anomaly (SSPSA; Area 1a). The SSPSA trends WNW, parallel to the most proximal portion of the 550-km-depth contour of the Pacific Plate along the Izu-Bonin trench. This region corresponds to the location where a \sim 100 km-thick subducted slab is expected to reach the base

of the MTZ (Lee *et al.* 2014; Sun *et al.* 2022). The mean d410 and d660 depths in the SSPSA are 413 ± 8 km and 678 ± 6 km, respectively (Figure 3 and Figure S2). The d410 is deeper (\sim 420 km) in the northwest and shallower (\sim 410 km) in the southeast of the SSPSA, with localized depressions reaching 8 ± 3 km beneath the Korean Peninsula, indicating spatial heterogeneity. The d660 attains its greatest depth (\sim 690 km) in the southeastern portion of the SSPSA, directly beneath the Philippine Sea slab, where significant stagnation of the Pacific slab at the base of the MTZ is inferred (arrow 1 in Figure 4a).

Depression of both the d410 and d660 is consistent across multiple regional velocity models (EARA2024, Xi *et al.* 2024; FWEA18; Tao *et al.* 2018) and a global model (TX2019slab; Lu *et al.* 2019), implying that these features are not artefacts of velocity corrections. The MTZ thickness is 264 ± 10 km (Figure 5), thickening towards the southeast (\sim 270 km) and thinning towards the northwest (\sim 260 km). Cross-sectional profiles along BB' and FF' (Figures 4b,f, respectively) illustrate the broad depression of both discontinuities across the SSPSA.

4.1.1.2. Northern stagnant Pacific Slab Anomaly.

The Northern Stagnant Pacific Slab Anomaly (NSPSA; Area 1b) exhibits patterns comparable to those of the SSPSA (Area 1a), featuring a significantly depressed d660 (680 ± 8 km) and a moderately depressed d410 (422 ± 6 km) (Figures 3 and 4d). The approximately north-trending portion of the 550-km-depth contour of the Pacific Plate lies within the NSPSA. The MTZ thickness is 258 ± 7 km, which exceeds the global average and reflects a more substantial depression of the d660 relative to the d410, consistent with prior observations of an anomalously deep d660 in this region (Ai *et al.* 2003; Li and Yuan 2003; Li *et al.* 2008; Liu *et al.* 2015, 2016; Zhang *et al.* 2016). Although the NSPSA lies in an area of relatively sparse ray coverage compared to the SSPSA (Figure 2), the number of piercing points still exceeds 50, ensuring sufficient stacking stability. The coincident depression of both d410 and d660 is consistent with the results obtained using different velocity models in this study (Figure S3) and with previous studies (e.g. Sun *et al.* 2020).

4.1.2. Southern Honshu Anomaly

In the Southern Honshu Anomaly (SHA; Area 2), a NNW-SSE trending zone beneath southernmost Honshu (31° – 37° N, 133° – 138° E), the d410 is elevated; the average depth is 392 ± 8 km (Figure 3a). The eastern boundary

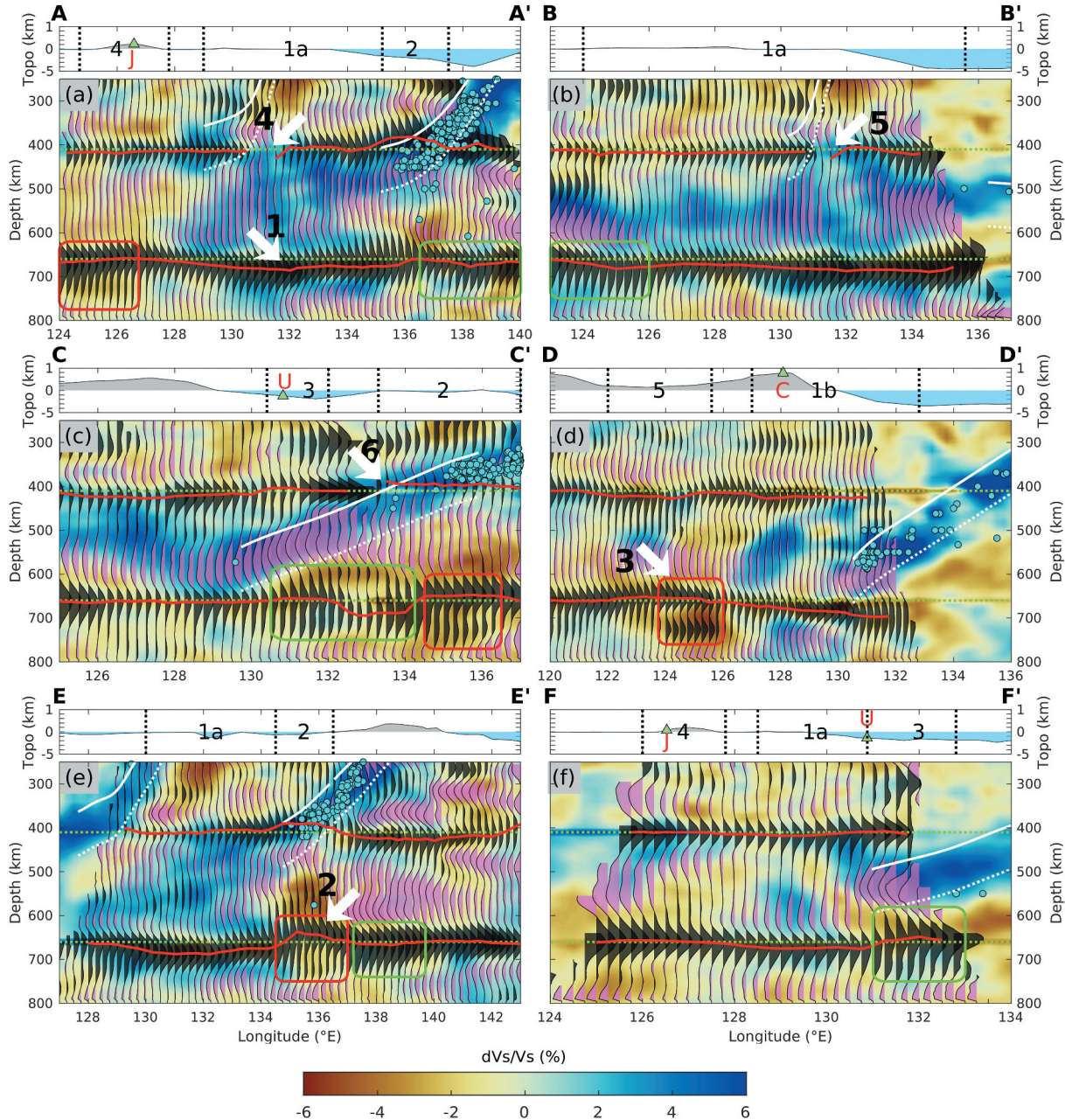


Figure 4. Cross-sections of CCP-stacked RFs across profiles AA'-FF' (a-f) with a corner frequency of 0.2 Hz ($\alpha = 0.4$ rad/s). Black-filled P_d s arrivals indicate positive amplitudes and magenta-filled arrivals indicate negative amplitudes. The background colour shows V_p perturbations from the EARA2024 model (Xi *et al.* 2024), according to the key below. Cyan circles mark hypocentre locations of earthquakes with depths <500 km between 2000 and 2010, and depths >500 km between 1964 and 2010 (International Seismological Centre 2024) that mark subducting slabs. Numbered white arrows highlight features discussed in the main text. Green dotted lines indicate the 410 km and 660 km isodepth lines, while red lines show the d410 and d660 variations observed in this study. White solid and dotted lines represent the top and bottom interfaces of the subducting oceanic plates (Pacific and Philippine Sea plates), respectively, assuming a plate thickness of 100 km. The top panel in each subplot displays land topography and bathymetry along each cross-section. Green triangles mark the locations of Cenozoic intraplate volcanoes. Black dotted vertical lines and labels (1a, 1b, 2, 3, 4, and 5) indicate the five subareas discussed in this study.

of this uplift roughly coincides with the 300-km-depth contour of the subducted Pacific slab, where the slab (~100 km thick) encounters the d410. Similar d410 uplift has been reported in previous RF studies (Niu *et al.* 2005;

Tonegawa *et al.* 2005; Lee *et al.* 2014). In this location, the d660 is depressed but shows localized shallowing (649 ± 5 km) in the central SHA, at around 35°N latitude and $135^\circ\text{--}137^\circ\text{E}$ longitude (arrow 2 in Figure 4e).

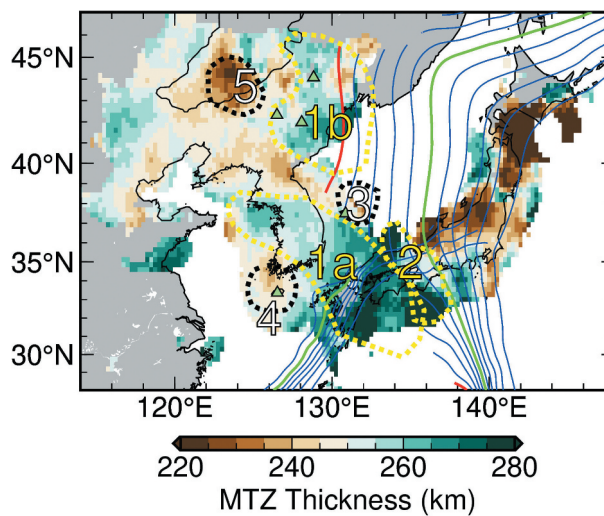


Figure 5. MTZ thicknesses estimated from the d410 and d660 topographies shown in Figure 3 ($a = 0.4 \text{ rad/s}$). Green triangles show locations of Holocene intraplate volcanic fields in East Asia. All other symbols and notations are the same as those of Figure 3.

4.1.3. Ulleung Anomaly

In the vicinity of Ulleung Island (U in Figure 1) in the East Sea (Sea of Japan), we observe the d410 at $409 \pm 7 \text{ km}$ and the d660 at $655 \pm 3 \text{ km}$, in the Ulleung Anomaly (UA; Area 3), as shown in Figures 3, 4c, and 4f. These depths are near the global averages, as is the MTZ thickness of $245 \pm 8 \text{ km}$ (Figure 5). The d660 is $\sim 25 \text{ km}$ shallower beneath the UA than under the neighbouring SSPSA (Area 1a) and NSPSA (Area 1b) that lie along the 550-km-depth contour of the Pacific slab (Figure 3). Consequently, the MTZ thickness of the UA is thinner than that of the NSPSA and SSPSA, which instead show $\sim 10\text{--}15 \text{ km}$ thickening.

4.1.4. Jeju Anomaly

In the Jeju Anomaly (JA; Area 4) beneath Jeju Island (J in Figure 1), the d410 is slightly depressed ($414 \pm 4 \text{ km}$) and the d660 is of near-average depth ($660 \pm 2 \text{ km}$) (Figures 3, 4a,f). The d410 is deeper in the northern JA, beneath Jeju Island, than in the southern part, which is closer to the subducting Philippine Sea Plate. The MTZ thickness is $246 \pm 4 \text{ km}$ (Figure 5). Notably, the d660 is shallower beneath the JA than under the neighbouring SSPSA (Area 1a).

4.1.5. Songliao Anomaly

In the Songliao Anomaly (SA; Area 5) of the southern Songliao Basin west of Changbaishan/Baekdu-san ($42^\circ\text{--}45^\circ\text{N}$, $122^\circ\text{--}126^\circ\text{E}$), the d660 is moderately uplifted, accompanied by depression of the d410. The d660 depths are $656 \pm 3 \text{ km}$ (Figure 3b) and those of the d410 are $422 \pm 5 \text{ km}$ (Figure 3a). The MTZ thickness is

thus reduced to $234 \pm 7 \text{ km}$. Such thinning is clearly evident in cross-section DD' (Figure 4d). Notably, the d660 is characterized by double Pds arrivals, with the later arrivals occurring at depths of $\sim 730 \text{ km}$ between longitudes 124°E and 126°E (arrow 3 in Figure 4d).

4.2. Amplitudes of the Pds from d410 and d660

Our observations reveal spatially heterogeneous P410s and P660s amplitudes across the study area (Figure 6). Uncertainties in converted wave amplitudes of P410s and P660s are low (< 0.005) in most areas, with the exception of a few localized regions, including the Liaodong Peninsula at 40°N and 121°E (~ 0.05) for the P410s (Figure 6c) and the central SA (Area 5) for the P660s (Figure 6d). Notably, these amplitude variations do not consistently correlate with the discontinuity depth variations (Figure 3). For instance, relatively low P410s amplitudes (1–2% of the P-wave amplitude) are observed beneath the central-to-northern Korean Peninsula, including the NSPSA (Area 1b) and the northwestern SSPSA (Area 1a). Reduced P410s amplitudes are also observed in the western SHA (Area 2). The P660s amplitudes similarly exhibit significant heterogeneity, with relatively low values (2–4% of the P amplitude) under the central-northern Korean Peninsula, including the northern SSPSA (Area 1a) and the NSPSA (Area 1b).

Cross-sectional images from the CCP stacks further show that diminished P410s amplitudes are particularly evident in regions where subducting slabs interact with the MTZ discontinuities. Specifically, along cross-sections AA' and BB' (arrows 4 and 5 in Figure 4a,b), reduced P410s amplitudes are observed where the Philippine Sea Plate interacts with the d410 ($131^\circ\text{--}132^\circ\text{E}$). Similarly, along cross-section CC' (arrow 6 in Figure 4c), reduced P410s amplitudes are observed in the SHA east of 133°E (Area 2), coinciding with the region where the Pacific Plate subducts into the MTZ. Notably, the spatial patterns of diminished P410s amplitudes differ between the two subduction systems: in the case of the Philippine Sea Plate, the amplitudes diminish at the trailing edge of the subducting slab (arrows 4 and 5 in Figure 4a,b), while for the Pacific Plate, the amplitudes diminish where the leading edge of the subducting plate encounters the d410 (arrow 6 in Figure 4c).

4.3. Multi-frequency Pds analyses

CCP stacked profiles at 0.2 Hz and 0.5 Hz reveal structural heterogeneity in the MTZ discontinuities. Multiple converted phases associated with the d410 and d660 interfaces are observed (Figures 4 and 7). Doubled positive Pds arrivals from the d660 are most apparent at the

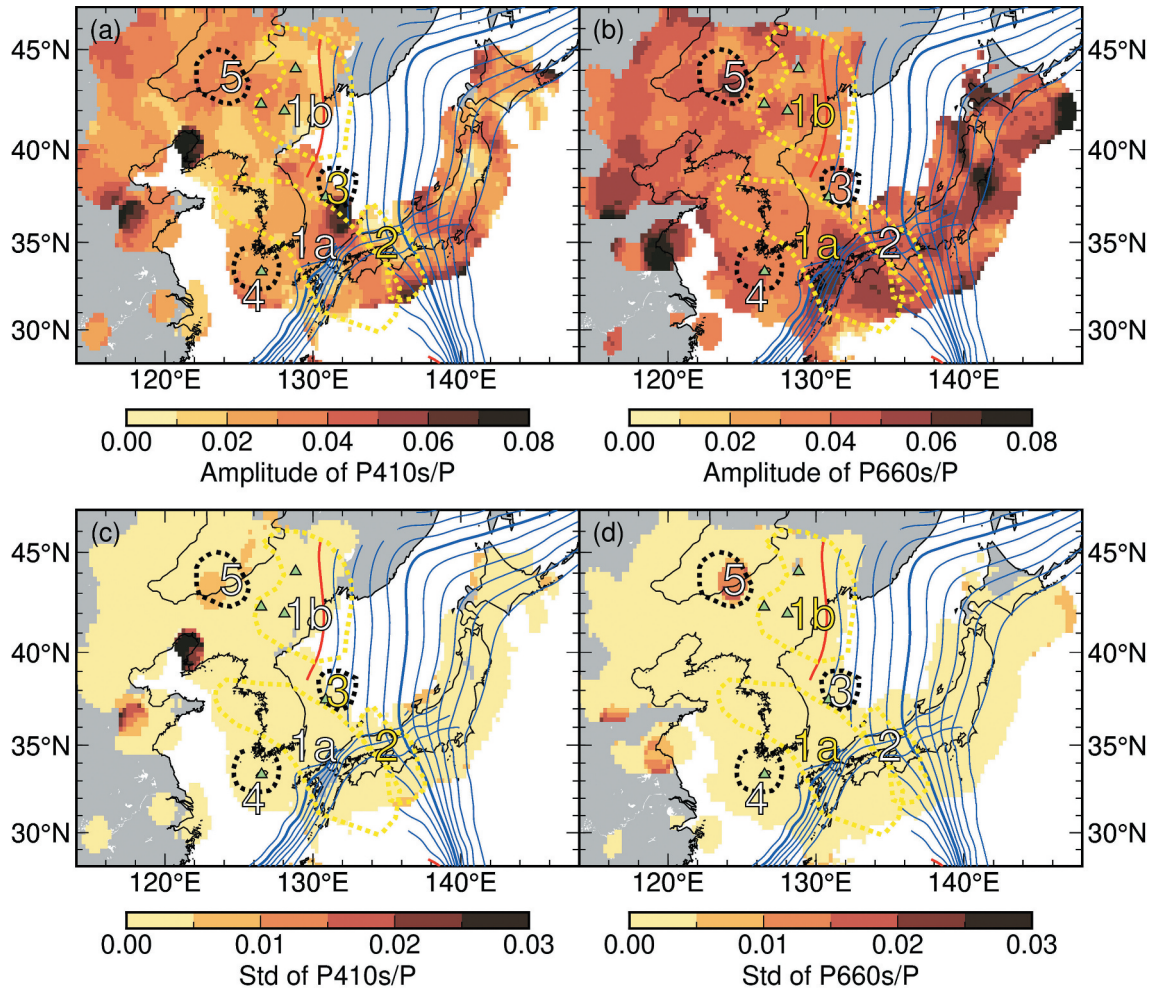


Figure 6. Amplitudes of the P_{ds} conversions from d410 (a) and d660 (b). Bootstrap uncertainties of the d410 (c) and d660 (d) amplitudes. Amplitudes are corrected for ray-parameter dependence to remove the influence of incidence angle and are displayed only in areas where hit counts exceed 50. All other symbols and notations are the same as those of Figure 3.

margins of the SSPSA (Area 1a) and NSPSA (Area 1b), where d660 is depressed. Strong later-arriving positive phases are observed at a depth of about 750 km in regions that exhibit slow- V_S anomalies in the EARA2024 model (red boxes in Figure 4a,c,d and e). The high-frequency RF images further resolve the broad low-frequency $P660s$ signals into multiple, sharper peaks (green boxes in Figures 4 and 7). Such complex features are predominantly found near the base of the subducting slab.

5. Discussion

5.1. Uncertainty of the MTZ model

5.1.1. Uncertainty from choice of velocity models in CCP migration

Uncertainties in the observed MTZ discontinuity depths and amplitudes largely stem from the choice of velocity

models used in the CCP migration (Figures S3–S4). To evaluate these uncertainties, we constructed CCP stacks using the 1D IASP91 model (Kennett and Engdahl 1991; Figure S5) and compared these to stacks generated from two regional 3D velocity models, FWEA18 (Tao *et al.* 2018; Figure S6) and EARA2024 (Xi *et al.* 2024; Figure 4), and a global 3D velocity model, TX2019slab (Lu *et al.* 2019; Figure S7).

The d410 depths from the IASP91 model are generally deeper than those obtained with the EARA2024 model between $\sim 125^\circ\text{E}$ and 135°E , whereas shallower depths are observed at longitudes west of 125°E and east of 138°E (Figures 3, S3a, and S4a). This discrepancy is likely attributable to strong negative V_S perturbations (up to 4–5%) at depths shallower than 100–200 km between $\sim 125^\circ\text{E}$ and 135°E in the 3D model (Xi *et al.* 2024). The d660 depths based on the IASP91 model are generally shallower than those from the EARA2024 model at longitudes west of 138°E (Figures S3b and S4b). This

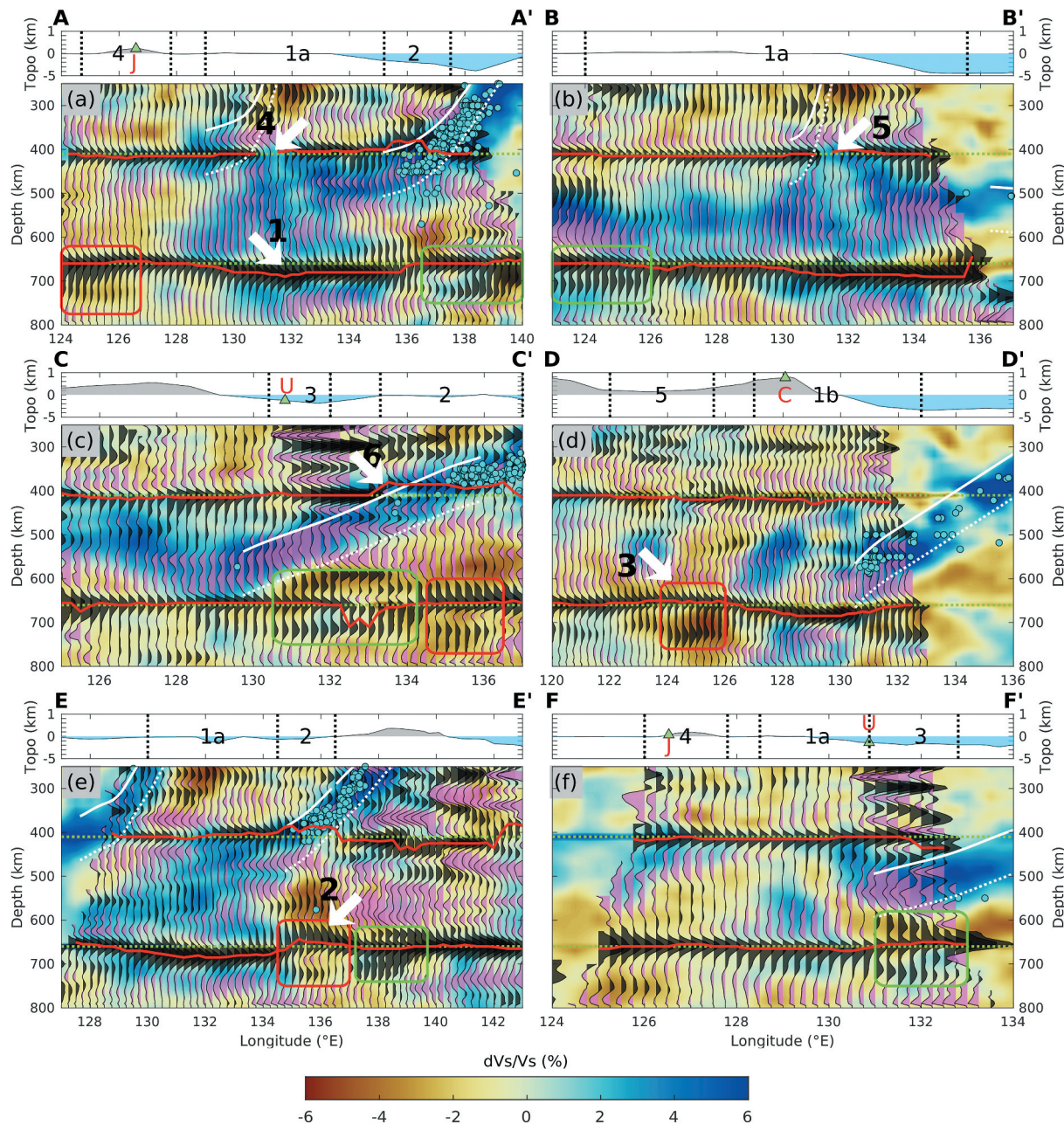


Figure 7. Cross-sections of CCP-stacked RFs along profiles AA'-FF' (see Figure 3a,b), constructed with a corner frequency of 0.5 Hz ($a = 1 \text{ rad/s}$). The background colour represents V_s perturbations from the EARA2024 model (Xi *et al.* 2024), according to the key below. All other symbols and notations are the same as those of Figure 4.

discrepancy is primarily due to the pronounced negative V_s anomalies at depths of $<100\text{--}200$ km between $\sim 125^\circ\text{E}$ and 135°E as well, in addition to moderate negative anomalies ($\sim 2\%$) at $400\text{--}600$ km depths beneath the northwestern Korean Peninsula near the SA (Area 5). These depth variations highlight the lateral heterogeneities in upper mantle structure that are not accounted for in the 1D velocity model.

Because the differences in available seismic velocity anomalies also affect our estimates of the depths to the MTZ phase transitions, we recalculated those

depths for each model (Figure S4). The average depth differences resulting from the EARA2024 and FWEA18 models are -1 ± 4 km for the d410 (Figure S4c), and -2 ± 4 km for the d660 (Figure S4d), resulting in an MTZ thickness difference of 1 ± 6 km across the study area. When compared with the global 3D model (TX2019slab), the EARA2024 model yields average depth differences of -2 ± 5 km for the d410 (Figure S4e), -4 ± 6 km for the d660 (Figure S4f), and 2 ± 7 km for the MTZ thickness. Note that the absolute depth estimates derived from different

velocity models are, on average, the same to within the quoted standard deviations. Localized discrepancies likely reflect lateral heterogeneities of varying magnitudes and spatial extents, influenced by differences in datasets, model assumptions, and inversion schemes among the velocity models used.

In addition, although the use of multiple velocity models yields broadly consistent results, it should be noted that seismic tomography models in general are subject to limited resolution and imperfect amplitude recovery, particularly for upper-mantle low-velocity anomalies (e.g. Hung *et al.* 2004; Rawlinson *et al.* 2014). This intrinsic limitation represents an additional source of uncertainty in the absolute depth estimates of MTZ discontinuities, regardless of the specific velocity model adopted.

5.1.2. Uncertainty from uneven data coverage in Northeastern China

The spatial distribution of seismic stations across East Asia is highly heterogeneous, resulting in uneven data coverage and lateral variations in the density of piercing points used for CCP stacking (Figure 2). This uneven coverage introduces additional uncertainty in the CCP images, as areas with sparse piercing points tend to produce less stable stacked amplitudes and may smear or obscure weak discontinuity signals. To assess such potential bias, we compared our results to those of two previous regional RF studies that achieved broader station coverage across mainland China (Sun *et al.* 2020; L. Liu *et al.* 2022). L. Liu *et al.* (2022) reported depression of the d660 (up to ~37 km) beneath the eastern part of the North China Craton (112° – 122° E, 29° – 42° N), which they attributed to a relatively large amount of water in the MTZ. The observation is generally consistent with our finding of a deep d660 west of 122° E and between 34° and 40° N, despite the relatively low sampling density in that region.

Sun *et al.* (2020) identified three approximately N–S elongated zones of significantly thickened MTZ beneath northeast Asia, which they associated with the thermal influence and dehydration of subducted slabs. Our observation of a thick MTZ beneath the northeastern Korean Peninsula (NSPSA, up to ~275 km) and near $\sim 120^{\circ}$ N and 35° N corresponds well with two of these elongated zones. However, the easternmost thick MTZ anomaly ($>135^{\circ}$ E) and the western extension of the thick MTZ ($<118^{\circ}$ E) reported by Sun *et al.* (2020) are not observed in our dataset, likely due to limited data coverage in these regions.

5.1.3. Uncertainty analysis from bootstrapping of CCP stacks

We performed bootstrap resampling to evaluate the uncertainty of the MTZ model constructed with the EARA2024 model (Xi *et al.* 2024). Specifically, we conducted CCP stacking over 1000 iterations using random selections of 70% of all RFs that pierced each bin in the stack. The standard deviation from bootstrapping for the d410 depths ranges between 1 and 23 km (Figure 3c), while that for the d660 depths ranges between 3 and 27 km (Figure 3d). The bootstrap uncertainty of d410 is relatively high (~10 km) for the Liaodong Peninsula (122° E, 40° N; west of point B) and even higher (~20 km) for northeastern Honshu Island (west of point E'; Figure 3c). For d660, the uncertainty is high (~20 km) to the north of the SA (Area 5) and south of Kyushu Island (Figure 3d). Uncertainty is moderately high (<15 km) for the northeastern NSPSA (Area 1b) and west of northern Honshu. Given such uncertainties, we exclude these regions from our interpretation.

5.2. Double-depressed d410 and d660 in the SSPSA and NSPSA

The co-occurrence of depressed d410 and d660 discontinuities in both the Korean Peninsula sector of the SSPSA (Area 1a) and the NSPSA (Area 1b) provides key constraints on the thermal and compositional influences within the MTZ. In the NSPSA, the presence of deep seismicity extending below 500 km indicates the presence of a cold subducting Pacific slab within the MTZ. Although such deep seismicity is absent in the SSPSA, persistent high-velocity anomalies imaged in multiple seismic tomography models (e.g. Tao *et al.* 2018; Xi *et al.* 2024) suggest the presence of the slab within the MTZ in this area. These observations collectively imply that low temperatures associated with the stagnant Pacific slab principally control the MTZ structure in both regions.

To evaluate the thermal contribution to the observed topography of the MTZ discontinuities beneath East Asia, we applied the thermodynamic relationship between MTZ thickness and temperature, as formulated by Helffrich (2000). The observed average MTZ thicknesses in the SSPSA (Area 1a) (264 ± 10 km) and NSPSA (Area 1b) (258 ± 7 km) yield temperature anomalies of -87 ± 60 K (1σ) and -46 ± 45 K (1σ), respectively (Figure 8 and Figure S2). However, they are less than the -300 to -700 K range of anomalously low temperatures commonly attributed to the Pacific slab (e.g. Kawakatsu and Yoshioka 2011).

To better estimate the slab's local thermal effect, we separately evaluated the thermal anomalies implied by

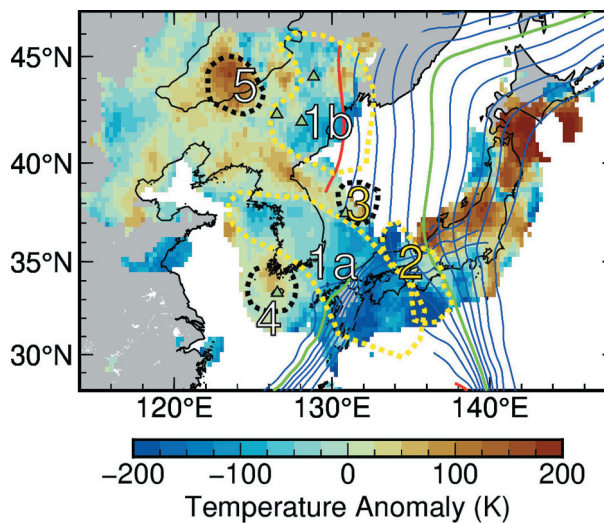


Figure 8. MTZ temperature anomaly estimates ($a = 0.4 \text{ rad s}^{-1}$).

the observed ~ 20 km depression of the d660. The ~ 20 km depression of the d660 can be explained by a cold temperature anomaly (-270 K), assuming a Clapeyron slope of -2.6 MPa/K for the d660 (Akaogi *et al.* 2007). This estimate is consistent with a thermal anomaly of -300 to -700 K typically attributed to the Pacific slab (e.g. Kawakatsu and Yoshioka 2011). For comparison, a ~ 20 km uplift of the d410 in SHA (Area 2), where the slab begins to penetrate the MTZ, corresponds to a -230 K thermal anomaly using a $+3.1 \text{ MPa/K}$ for the d410 (Akaogi *et al.* 2007).

A purely thermal model of a cold slab, however, cannot fully explain the observed morphology. A cold slab should thicken the MTZ by elevating the d410 and depressing the d660, given their opposing Clapeyron slopes. Yet, both discontinuities are depressed, deviating from this expected cold, thermally driven response. This discrepancy suggests that while the cold stagnant slab dominantly influences the d660, additional factors, such as elevated temperatures or other compositional heterogeneities (e.g. water and carbon), may also contribute to the depression of the d410.

5.2.1. Depressed d410 in the NSPSA

A purely thermal explanation for the ~ 10 km depression of the d410 in the SSPSA and NSPSA (Areas 1a and 1b) would require a local positive thermal anomaly of approximately $+110$ K. This implies that the influence of the cold slab is primarily confined to the lower MTZ (near the d660), while the upper MTZ (near the d410) may be affected by additional thermal or compositional factors.

Thermal upwelling may contribute to the d410 depression beneath the NSPSA (Area 1b). This region

includes the Changbaishan/Baekdu-san volcano, where Tian *et al.* (2016) reported broad depressions of both d410 and d660. They attributed these features to hot mantle upwelling affecting the d410, in association with a slow-velocity anomaly imaged down to 410 km depth beneath the volcano (Zhao *et al.* 2009), and to the cold stagnant Pacific slab depressing the d660. In our CCP cross-section (Figure 4d), an oblique continuation of a slow-velocity anomaly is observed extending across SA (Area 5) and NSPSA (Area 1b) in the EARA2024 tomography model (Xi *et al.* 2024). This structure coincides with an uplifted d660 beneath SA (Area 5) and a depressed d410 beneath NSPSA (Area 1b), suggesting an oblique hot upwelling that originates from the lower mantle and locally affects the upper MTZ boundary. A $\sim 1\%$ slow- V_s anomaly at the d410 depth corresponds to a thermal anomaly of ~ 100 K, assuming that the anomaly is purely temperature-related (Cammarano *et al.* 2003). This would yield a ~ 10 km depression, consistent with our observation.

5.2.2. Depressed d410 in the SSPSA

In contrast, a purely thermal explanation for the d410 depression in the Korean Peninsula sector of the SSPSA (Area 1a) appears insufficient, and compositional factors are likely required. No slow-velocity anomaly that could be linked to a plume or mantle upwelling is apparent in the MTZ beneath this region (Figure 4b). The regional tomography beneath the Korean Peninsula shows slow- V_p structures shallower than ~ 300 km beneath its southeastern part, interpreted as evidence for elevated upper mantle temperatures (Song *et al.* 2020). However, the vertical and horizontal extents of this anomaly are too limited to explain the widespread d410 depression. Specifically, the SSPSA (Area 1a) spans the entire southern Korean Peninsula, not merely its eastern portion.

An alternative interpretation involves the impact of hydration on the seismic detectability of the d410. Hydrated wadsleyite has been proposed to be chemically buoyant relative to its anhydrous counterpart and may remain stable near the top of the MTZ (Karato 2006). When H_2O concentrations exceed ~ 0.75 wt.%, the seismic impedance contrast between olivine and hydrous wadsleyite at the d410 decreases, making the boundary more difficult to detect (Schmerr and Garnero 2007). In this context, the boundary between hydrated and dry wadsleyite at greater depths may appear as a depressed d410, although it does not represent the actual olivine-wadsleyite phase transition. This mechanism has been invoked to explain similar double-depressed discontinuities where the Nazca Plate subducts beneath South America (Schmerr and Garnero 2007) and was also

suggested to occur beneath the East Asian cratonic margin (Lee *et al.* 2014).

In addition to hydration, significant changes in carbon solubility between olivine and wadsleyite may contribute to the depression of the d410 under cold MTZ conditions. Experimental studies have shown that olivine can incorporate significantly more carbon than its high-pressure polymorph wadsleyite under upper mantle and transition zone conditions (Shcheka *et al.* 2006). This implies that, when the mantle is carbon-rich, olivine may be thermodynamically stabilized over a broader pressure–temperature range. As the stability of mantle phases can be influenced by their capacity to host volatile components (Frost and Dolejš 2007), elevated carbon concentrations could shift the olivine–wadsleyite phase boundary to higher pressures, potentially resulting in a depressed d410. This mechanism provides a plausible explanation for the observed d410 depression in cold, volatile-rich subduction settings, where carbon derived from subducting slabs may accumulate near the top of the MTZ (Thomson *et al.* 2016; S.-A. Liu *et al.* 2022).

5.3. Complexity in the MTZ discontinuity structure

5.3.1. Lateral variations in Pds amplitudes: possible evidence of compositional heterogeneity

Our RF results show that converted wave amplitudes (both P410s and P660s) exhibit pronounced lateral variability on scales of ~ 200 km (Figure 6). These variations reflect differences in the seismic impedance contrast, which depends on both velocity and density differences across the conversion boundary. However, their spatial patterns show little correlation with variations in discontinuity depths (Figure 3a,b), yielding negligible coefficients ($|r| < 0.06$). Because the depth variations are primarily controlled by thermal structure, this lack of correlation implies that additional factors, such as compositional heterogeneity or hydration, likely contribute to the observed amplitude variations.

Previous mineral physics studies have shown that impedance contrasts across the d410 and d660 are sensitive to mantle composition, with higher basaltic content generally reducing impedance contrasts (Duffy and Anderson 1989; Vacher *et al.* 1998; Xu *et al.* 2008). Seismological studies using precursor phases have also inferred significant basaltic enrichment in the MTZ beneath East Asia, with estimates of basaltic fraction reaching $\sim 0.5\text{--}0.6$ (Tauzin *et al.* 2022; Waszek *et al.* 2024). Although direct quantitative calibration between P-to-S amplitudes and basalt fraction is not yet available, our observations are qualitatively consistent with the interpretation that compositional heterogeneity,

including possible basalt enrichment, influences MTZ seismic properties. Future work involving mineral physics modelling and waveform analyses will be essential to quantify these compositional effects more rigorously.

5.3.2. Multiple discontinuities near d660

Our CCP cross-sections highlight the complexity of the MTZ structure beneath East Asia. Notably, we observe paired positive Pds arrivals from the d660 at depths of about 660 km and 750 km, particularly beneath regions associated with slow-velocity anomalies in tomography models. Similar observations of double d660 phases and deepened discontinuities beneath subduction zones have been reported previously (Zang *et al.* 2006; Tibi *et al.* 2007). These arrivals imply the presence of two distinct impedance contrasts near the base of the MTZ.

Broad and smooth P660s amplitudes observed in lower-frequency RF images are resolved into multiple sharp P660s phases in higher-frequency RF images (green boxes in Figures 4 and 7). These features are predominantly located near the base of subducting slabs, suggesting localized structural or compositional heterogeneity. These observations emphasize that the MTZ discontinuity near 660 km depth is often not a single, continuous boundary, but rather comprises a series of sharp, closely spaced layers with high impedance contrasts, possibly reflecting multiple phase transitions or layering in subducted material (Andrews and Deuss 2008).

One possible explanation for the secondary interface at ~ 750 km is a phase transition involving minerals that are not part of the olivine group. While the discontinuity at ~ 660 km is primarily due to the ringwoodite-to-bridgmanite and ferropericlase transitions, seismic and experimental studies suggest that majorite garnet may also transform to perovskite at these depths under elevated thermal conditions (Hirose 2002; Deuss *et al.* 2013). Hot or warm asthenospheric material entrained by the stagnant slab could have created locally elevated thermal conditions, potentially allowing garnet phase transitions to occur at these depths.

5.4. Intraplate volcanic activity beneath Ulleung and Jeju in East Asia

The MTZ structures beneath Ulleung (UA) and Jeju Islands (JA) share notable similarities. Both regions exhibit near-global average depths of the d660, suggesting limited influence from the cold, stagnant Pacific slab. Specifically, the d660 lies about 20 km shallower than in adjacent slab-affected regions (SSPSA and NSPSA), likely reflecting variations in slab geometry, hydration state, or localized thermal perturbations.

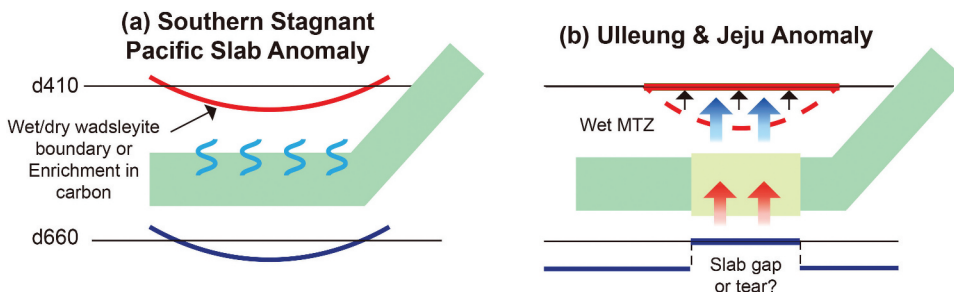


Figure 9. Schematic of MTZ processes beneath (a) the Southern Stagnant Pacific Slab Anomaly (SSPSA) and (b) the Ulleung and Jeju Anomaly (UA and JA). (a) In the SSPSA, the depressed d660 likely reflects the influence of the cold, stagnant Pacific slab; above the stagnant slab, the depressed d410 beneath the Korean Peninsula sector of the SSPSA may result from hydrous enrichment that produces an interface between wet and dry wadsleyite, or from carbon enrichment. Such volatiles may be sourced from the stagnant slab. (b) The near-normal d660 depths beneath the UA and JA suggest limited influence from the cold stagnant slab, possibly due to a slab gap or tear. Mantle upwelling through such a tear is likely hydrous rather than purely thermal, which can explain the near-normal d410 depths. For comparison, the red dashed curve illustrates the expected depression of the d410 in the case of purely thermal upwelling.

Several tomographic studies have suggested that a slab gap or tear may exist in the stagnant Pacific slab. Obayashi *et al.* (2009, 2013) identified a vertical tear in the Pacific slab beneath central Honshu ($\sim 35^\circ$), which may extend westward towards the Korean Peninsula. More recent tomographic models (e.g. Y.-W. Kim *et al.* 2021; Xi *et al.* 2024) also suggest a possible slab gap or tear beneath Jeju, with one model revealing a low-velocity anomaly extending to the base of the MTZ (Y.-W. Kim *et al.* 2021), interpreted as mantle upwelling through the tear. If present, such a slab tear could provide a pathway for buoyant mantle material to ascend and undergo decompression melting, thereby generating intraplate volcanism. Geochemical analyses from Ulleung and Jeju volcanic rocks indicate contributions from hydrous or hydrothermally altered components derived from the MTZ (Choi 2021; Kim and Choi 2025), consistent with hydration-enhanced buoyancy of upwelling material. Numerical models further show that a critical concentration of water (0.2–0.3 wt.%) can accumulate in the MTZ beneath northeast Asia (Yang and Faccenda 2020), facilitating hydrous upwelling.

Conversely, several observations imply that the Pacific slab may be continuous beneath both islands. Deep-focus earthquakes (>500 km) near Ulleung indicate slab continuity, and the tear proposed beneath southwest Japan cannot be confidently linked to Ulleung due to limited data coverage in the East Sea. Other tomography models (e.g. FWEA18 (Tao *et al.* 2018), EARA2024 (Xi *et al.* 2024), and TX2019slab (Lu *et al.* 2019)) also provide no clear evidence of tearing beneath Ulleung.

Assuming that the slab is continuous, the near-normal d660 is particularly noteworthy. The presence

of a cold slab would normally deepen the d660 by ~ 20 km, as observed in nearby slab-affected regions (NSPSA and SSPSA), equivalent to a thermal effect of about -270 K. Therefore, maintaining a near-normal depth requires a compensating positive thermal perturbation of ~ 270 K near the MTZ base. Such a temperature excess indicates that the mantle beneath Ulleung and Jeju is considerably warmer than the surrounding slab-affected areas. The observed double reflector around ~ 750 km beneath Jeju may represent the garnet-perovskite transition under elevated temperatures (e.g. Hirose 2002; Jenkins *et al.* 2016).

Thermal effects aside, local slab buckling (Lee *et al.* 2014) or hydration variations could further modulate the d660 depths. However, extreme slab curvature is not well supported by current tomography or slab models, and geochemical evidence favours hydrous rather than dry mantle conditions (Moon *et al.* 2020; Choi 2021). Considering the water budget of subducted oceanic crust (e.g. Kelbert *et al.* 2009), an extremely dry MTZ is unlikely.

While the near-normal d410 could simply reflect unperturbed thermochemical MTZ conditions, an alternative interpretation is that the upwelling mantle beneath UA and JA is not significantly hotter than the ambient mantle but is instead buoyant because of hydration near d410. In this case, the absence of d410 depression may reflect the influence of a hydrous, rather than thermal, upwelling – a scenario consistent with models of water-rich MTZs facilitating vertical flow without strong thermal anomalies (cf. Liu *et al.* 2023).

In summary, our RF results suggest that the cold, stagnant Pacific slab exerts limited influence beneath Ulleung and Jeju. This could reflect either a slab tear/gap or

a thermal anomaly at the MTZ base. The combination of a near-normal d410 and d660, tomographic low-velocity anomalies, and geochemical and geodynamic constraints is most consistent with hydrous upwelling from the MTZ. However, alternative explanations such as local slab buckling or a dry MTZ cannot be completely excluded.

5.5. Summary of the interpreted MTZ anomalies

Figure 9 shows a schematic summary of representative anomalies across the study area, illustrating our interpretations of regional variations in the MTZ structure. These features exemplify the complex and variable interplay of thermal and compositional processes that affect the seismic structure of the MTZ. Both the d410 and d660 are depressed beneath the Korean Peninsula sector of the SSPSA, but are near-normal beneath the UA and JA. The SSPSA reflects the combined effects of a cold, stagnant Pacific slab and enrichment in volatile components (water and carbon) (Figure 9a). In contrast, the near-normal d660 depths beneath the UA and JA indicate a limited influence from the cold stagnant slab, possibly because of a slab gap or tear (Figure 9b). Mantle upwelling through such a tear is likely hydrous rather than purely thermal near the d410, consistent with upwelling through a wet MTZ. Hydrous upwelling can shift the d410 to shallower depths, whereas purely thermal upwelling is expected to produce a depressed d410 (Chen *et al.* 2002). This provides a plausible explanation for the observed near-normal d410 depths beneath the UA and JA (Figure 9b).

6. Conclusions

Using high-resolution receiver function (RF) imaging from over 40,000 teleseismic *P*-to-*S* conversions, we present new constraints on the structure of the mantle transition zone (MTZ) beneath eastern China, the Korean Peninsula, and Japan, highlighting its complex thermochemical nature and its critical influence on intraplate volcanism. Multi-frequency RF images reveal significant lateral variations in both the depth and amplitude of the 410-km (d410) and 660-km (d660) seismic discontinuities across the region. These variations manifest as substantial regional variability in MTZ thickness and discontinuity topography that reflect the interplay of the thermal and compositional heterogeneities within the mantle.

The most prominent features revealed in this study include a broad depression of both d410 and d660 beneath the Korean Peninsula, associated with the cold, stagnant Pacific slab, likely enriched in water and carbon. Multiple reflectors observed near

the d660, and in particular, doubled seismic discontinuities, are likely related to garnet phase transitions under elevated temperatures. The MTZ structure beneath Cenozoic intraplate volcanic regions of Ulleung and Jeju implies limited influence from the stagnant Pacific slab, potentially reflecting a slab tear or a localized thermal anomaly near the base of the MTZ. The inferred mantle upwelling through such a tear is more plausibly hydrous rather than purely thermal, consistent with the near-normal depth of the d410 beneath these regions. These features, along with heterogeneous *Pds* amplitudes, support the presence of compositional heterogeneity such as basaltic enrichment within parts of the MTZ. Future studies that integrate RF imaging with mineral physics and geodynamic modelling will further clarify the link between the deep mantle structure and surface magmatic processes across East Asia.

Acknowledgments

The authors thank Sung Keun Lee (Seoul National University) and Eun Jeong Kim (Kongju National University) for their valuable comments on carbon and akimotoite enrichment in the MTZ. We are also grateful to the Editors and two anonymous Reviewers for their constructive comments.

Disclosure statement

No potential conflict of interest was reported by the author(s).

Funding

This work was supported by the National Research Foundation of Korea (NRF) Grant RS-2022-NR070842 to H. Kang and Y. Kim and NRF Grant RS-2023-00245550 to H. Kang.

Author contributions

Conceptualization: YK
 Data Curation: HK
 Formal Analysis: HK
 Funding Acquisition: HK, YK
 Investigation: HK, RMR, YK
 Methodology: HK, RMR, YK
 Project Administration: HK
 Resources: HK, RMR, YK
 Software: HK
 Supervision: RMR, YK
 Validation: HK
 Writing – original draft: HK
 Writing – review & editing: HK, RMR, YK



References

- Ai, Y., Zheng, T., Xu, W., He, Y., and Dong, D., 2003, A complex 660 km discontinuity beneath northeast China: *Earth and Planetary Science Letters*, v. 212, p. 63–71. doi: [10.1016/S0012-821X\(03\)00266-8](https://doi.org/10.1016/S0012-821X(03)00266-8)
- Ai, Y., Zheng, T., Xu, W., and Li, Q., 2008, Small scale hot upwelling near the north yellow sea of eastern China: *Geophysical Research Letters*, v. 35, p. L20305. doi: [10.1029/2008GL035269](https://doi.org/10.1029/2008GL035269)
- Akaogi, M., Takayama, H., Kojitani, H., Kawaji, H., and Atake, T., 2007, Low-temperature heat capacities, entropies and enthalpies of Mg_2SiO_4 polymorphs, and α – β – γ and post-spinel phase relations at high pressure: *Physics and Chemistry of Minerals*, v. 34, p. 169–183. doi: [10.1007/s00269-006-0137-3](https://doi.org/10.1007/s00269-006-0137-3)
- Ammon, C.J., 1991, The isolation of receiver effects from teleseismic P waveforms: *Bulletin of the Seismological Society of America*, v. 81, p. 2504–2510. doi: [10.1785/BSSA0810062504](https://doi.org/10.1785/BSSA0810062504)
- Andrews, J., and Deuss, A., 2008, Detailed nature of the 660 km region of the mantle from global receiver function data: *Journal of Geophysical Research: Solid Earth*, v. 113, p. B06304 doi: [10.1029/2007JB005111](https://doi.org/10.1029/2007JB005111)
- Bercovici, D., and Karato, S.I., 2003, Whole-mantle convection and the transition-zone water filter: *Nature*, v. 425, p. 39–44. doi: [10.1038/nature01918](https://doi.org/10.1038/nature01918)
- Bina, C.R., and Helffrich, G., 1994, Phase transition clapeyron slopes and transition zone seismic discontinuity topography: *Journal of Geophysical Research: Solid Earth*, v. 99, p. 15853–15860. doi: [10.1029/94JB00462](https://doi.org/10.1029/94JB00462)
- Bissig, F., Khan, A., and Giardini, D., 2022, Evidence for basalt enrichment in the mantle transition zone from inversion of triplicated P-and S-waveforms: *Earth and Planetary Science Letters*, v. 580, p. 117387. doi: [10.1016/j.epsl.2022.117387](https://doi.org/10.1016/j.epsl.2022.117387)
- Brenna, M., Cronin, S.J., Keresztsuri, G., Sohn, Y.K., Smith, I.E.M., and Wijbrans, J., 2015, Intraplate volcanism influenced by distal subduction tectonics at Jeju Island, Republic of Korea: *Bulletin of Volcanology*, v. 77, p. 1–16. doi: [10.1007/s00445-014-0896-5](https://doi.org/10.1007/s00445-014-0896-5)
- Brenna, M., Cronin, S.J., Smith, I.E., Sohn, Y.K., and Maas, R., 2012, Spatio-temporal evolution of a dispersed magmatic system and its implications for volcano growth, Jeju Island volcanic field, Korea: *Lithos*, v. 148, p. 337–352. doi: [10.1016/j.lithos.2012.06.021](https://doi.org/10.1016/j.lithos.2012.06.021)
- Brenna, M., Price, R., Cronin, S.J., Smith, I.E.M., Sohn, Y.K., Kim, G.B., and Maas, R., 2014, Final magma storage depth modulation of explosivity and trachyte–phonolite genesis at an intraplate volcano: A case study from Ulleung Island, South Korea: *Journal of Petrology*, v. 55, p. 709–747. doi: [10.1093/petrology/egu004](https://doi.org/10.1093/petrology/egu004)
- Cammarano, F., Goes, S., Vacher, P., and Giardini, D., 2003, Inferring upper-mantle temperatures from seismic velocities: *Physics of the Earth and Planetary Interiors*, v. 138, p. 197–222. doi: [10.1016/S0031-9201\(03\)00156-0](https://doi.org/10.1016/S0031-9201(03)00156-0)
- Castle, J.C., and Creager, K.C., 1998, Topography of the 660-km seismic discontinuity beneath Izu-Bonin: Implications for tectonic history and slab deformation: *Journal of Geophysical Research: Solid Earth*, v. 103, p. 12511–12527. doi: [10.1029/98JB00503](https://doi.org/10.1029/98JB00503)
- Chanyshhev, A., Ishii, T., Bondar, D., Bhat, S., Kim, E.J., Farla, R., Nishida, K., Liu, Z., Wang, L., Nakajima, A., Yan, B., Tang, H., Chen, Z., Higo, Y., Tange, Y., and Katsura, T., 2022, Depressed 660-km discontinuity caused by akimotoite–bridgmanite transition: *Nature*, v. 601, p. 69–73. doi: [10.1038/s41586-021-04157-z](https://doi.org/10.1038/s41586-021-04157-z)
- Chen, J., Inoue, T., Yurimoto, H., and Weidner, D.J., 2002, Effect of water on olivine-wadsleyite phase boundary in the $(Mg, Fe)_2SiO_4$ system: *Geophysical Research Letters*, v. 29, p. 22–1–22–4 doi: [10.1029/2001GL014429](https://doi.org/10.1029/2001GL014429)
- Chen, S.S., Lee, S.G., Lee, T.J., Lee, Y.S., and Liu, J.Q., 2018, Multi-stage magmatic plumbing system of the volcano: A case study from Ulleung Island, South Korea: *Lithos*, v. 314, p. 201–215. doi: [10.1016/j.lithos.2018.05.028](https://doi.org/10.1016/j.lithos.2018.05.028)
- Choi, S.H., 2021, Geochemistry and petrogenesis of quaternary volcanic rocks from Ulleung Island, South Korea: *Lithos*, v. 380, p. 105874 doi: [10.1016/j.lithos.2020.105874](https://doi.org/10.1016/j.lithos.2020.105874)
- Choi, S.H., Suzuki, K., and Senda, R., 2024, Rhenium–os isotopic systematics of late Cenozoic intraplate basaltic rocks from Korea: Implications for recycled slab materials in their mantle source: *Chemical Geology*, v. 668, p. 122330. doi: [10.1016/j.chemgeo.2024.122330](https://doi.org/10.1016/j.chemgeo.2024.122330)
- Collier, J.D., and Helffrich, G.R., 1997, Topography of the “410” and “660” km seismic discontinuities in the Izu-Bonin subduction zone: *Geophysical Research Letters*, v. 24, p. 1535–1538. doi: [10.1029/97GL01383](https://doi.org/10.1029/97GL01383)
- Deuss, A., Andrews, J., and Day, E., 2013, Seismic observations of mantle discontinuities and their mineralogical and dynamical interpretation, in Karato, S.-I., ed. *Physics and chemistry of the deep earth*: Hoboken, New Jersey, John Wiley & Sons, Ltd, pp. 295–323.
- Dueker, K.G., and Sheehan, A.F., 1997, Mantle discontinuity structure from midpoint stacks of converted P to S waves across the Yellowstone hotspot track: *Journal of Geophysical Research: Solid Earth*, v. 102, p. 8313–8327. doi: [10.1029/96JB03857](https://doi.org/10.1029/96JB03857)
- Duffy, T.S., and Anderson, D.L., 1989, Seismic velocities in mantle minerals and the mineralogy of the upper mantle: *Journal of Geophysical Research: Solid Earth*, v. 94, p. 1895–1912. doi: [10.1029/JB094iB02p01895](https://doi.org/10.1029/JB094iB02p01895)
- Frost, D.J., and Dolejš, D., 2007, Experimental determination of the effect of H_2O on the 410-km seismic discontinuity: *Earth and Planetary Science Letters*, v. 256, p. 182–195. doi: [10.1016/j.epsl.2007.01.023](https://doi.org/10.1016/j.epsl.2007.01.023)
- Fukao, Y., and Obayashi, M., 2013, Subducted slabs stagnant above, penetrating through, and trapped below the 660 km discontinuity: *Journal of Geophysical Research: Solid Earth*, v. 118, p. 5920–5938 doi: [10.1002/2013JB010466](https://doi.org/10.1002/2013JB010466)
- Fukao, Y., Obayashi, M., and Nakakuki, T., 2009, And deep slab project group, 2009, stagnant slab: A review: *Annual Review of Earth and Planetary Sciences*, v. 37, p. 19–46. doi: [10.1146/annurev.earth.36.031207.124224](https://doi.org/10.1146/annurev.earth.36.031207.124224)
- Ghosh, S., Ohtani, E., Litasov, K.D., Suzuki, A., Dobson, D., and Funakoshi, K., 2013, Effect of water in depleted mantle on post-spinel transition and implication for 660 km seismic discontinuity: *Earth and Planetary Science Letters*, v. 371–372, p. 103–111. doi: [10.1016/j.epsl.2013.04.011](https://doi.org/10.1016/j.epsl.2013.04.011)
- Han, G., Li, J., Guo, G., Mooney, W.D., Karato, S.I., and Yuen, D.A., 2021, Pervasive low-velocity layer atop the 410-km discontinuity beneath the northwest Pacific subduction zone: Implications for rheology and geodynamics: *Earth and Planetary Science Letters*, v. 554, p. 116642. doi: [10.1016/j.epsl.2020.116642](https://doi.org/10.1016/j.epsl.2020.116642)
- Hasterok, D., Halpin, J.A., Collins, A.S., Hand, M., Kreemer, C., Gard, M.G., and Glorie, S., 2022, New maps of global

- geological provinces and tectonic plates: *Earth-Science Reviews*, v. 231, p. 104069. doi: [10.1016/j.earscirev.2022.104069](https://doi.org/10.1016/j.earscirev.2022.104069)
- Hayes, G.P., Moore, G.L., Portner, D.E., Hearne, M., Flamme, H., Furtney, M., and Smoczyk, G.M., 2018, Slab2, a comprehensive subduction zone geometry model: *Science*, v. 362, p. 58–61. doi: [10.1126/science.aat4723](https://doi.org/10.1126/science.aat4723)
- Helffrich, G., 2000, Topography of the transition zone seismic discontinuities: *Reviews of Geophysics*, v. 38, p. 141–158. doi: [10.1029/1999RG000060](https://doi.org/10.1029/1999RG000060)
- Hirose, K., 2002, Phase transitions in pyrolytic mantle around 670-km depth: Implications for upwelling of plumes from the lower mantle: *Journal of Geophysical Research: Solid Earth*, v. 107, p. 2078. doi: [10.1029/2001JB000597](https://doi.org/10.1029/2001JB000597)
- Hung, S.H., Shen, Y., and Chiao, L.Y., 2004, Imaging seismic velocity structure beneath the Iceland hot spot: A finite frequency approach: *Journal of Geophysical Research: Solid Earth*, v. 109, p. B08305. doi: [10.1029/2003JB002889](https://doi.org/10.1029/2003JB002889)
- International Seismological Centre. 2024. On-Line bulletin. doi: [10.31905/D808B830](https://doi.org/10.31905/D808B830)
- Ito, E., and Takahashi, E., 1989, Postspinel transformations in the system Mg₂SiO₄-Fe₂SiO₄ and some geophysical implications: *Journal of Geophysical Research: Solid Earth*, v. 94, p. 10637–10646. doi: [10.1029/JB094iB08p10637](https://doi.org/10.1029/JB094iB08p10637)
- Jenkins, J., Cottaar, S., White, R.S., and Deuss, A., 2016, Depressed mantle discontinuities beneath Iceland: Evidence of a garnet controlled 660 km discontinuity?: *Earth and Planetary Science Letters*, v. 433, p. 159–168. doi: [10.1016/j.epsl.2015.10.053](https://doi.org/10.1016/j.epsl.2015.10.053)
- Karato, S., 2006, Water in the earth's mantle, in Keppler, H. and Smyth, J.R., eds. *Water in nominally anhydrous minerals*: St. Louis, Missouri, Geochemical Society, *Reviews in Mineralogy and Geochemistry*, Vol. 62, pp. 343–375.
- Katsura, T., and Ito, E., 1989, The system Mg₂SiO₄-Fe₂SiO₄ at high pressures and temperatures: Precise determination of stabilities of olivine, modified spinel, and spinel: *Journal of Geophysical Research: Solid Earth*, v. 94, p. 15663–15670. doi: [10.1029/JB094iB11p15663](https://doi.org/10.1029/JB094iB11p15663)
- Katsura, T., Yamada, H., Shinmei, T., Kubo, A., Ono, S., Kanazaki, M., Yoneda, A., Walter, M.J., Ito, E., Urakawa, S., Funakoshi, K., and Utsumi, W., 2003, Post-spinel transition in Mg₂SiO₄ determined by high P-T in situ X-ray diffractometry: *Physics of the Earth and Planetary Interiors*, v. 136, p. 11–24. doi: [10.1016/S0031-9201\(03\)00019-0](https://doi.org/10.1016/S0031-9201(03)00019-0)
- Kawakatsu, H., and Yoshioka, S., 2011, Metastable olivine wedge and deep dry cold slab beneath southwest Japan: *Earth and Planetary Science Letters*, v. 303, p. 1–10. doi: [10.1016/j.epsl.2011.01.008](https://doi.org/10.1016/j.epsl.2011.01.008)
- Kelbert, A., Schultz, A., and Egbert, G., 2009, Global electromagnetic induction constraints on transition-zone water content variations: *Nature*, v. 460, p. 1003–1006. doi: [10.1038/nature08257](https://doi.org/10.1038/nature08257)
- Kennett, B.L.N., 1983, Seismic wave propagation in stratified media: Cambridge, United Kingdom, Cambridge University Press, p. 342.
- Kennett, B.L.N., and Engdahl, E.R., 1991, Traveltimes for global earthquake location and phase identification: *Geophysical Journal International*, v. 105, p. 429–465. doi: [10.1111/j.1365-246X.1991.tb06724.x](https://doi.org/10.1111/j.1365-246X.1991.tb06724.x)
- Kim, D., Lee, H., Lee, W., Kim, J., Oh, J., Song, J.H., Jung, H., and Stuart, F.M., 2021, Helium isotopes and olivine geochemistry of basalts and mantle xenoliths in Jeju Island, South Korea: Evaluation of role of SCLM on the cenozoic intraplate volcanism in East Asia: *Lithos*, v. 390–391, p. 106123. doi: [10.1016/j.lithos.2021.106123](https://doi.org/10.1016/j.lithos.2021.106123)
- Kim, E.J., and Lee, S.K., 2025, Formation of structurally bound carbonate in silicate melts on the top of the mantle transition zone: *Geophysical Research Letters*, v. 52, p. e2024GL113755. doi: [10.1029/2024GL113755](https://doi.org/10.1029/2024GL113755)
- Kim, J.I., and Choi, S.H., 2025, Origin of low- $\delta^{18}\text{O}$ olivine phenocrysts in late Cenozoic EM2-type intraplate basalts from Jeju Island, South Korea: *Journal of Asian Earth Sciences*, v. 279, p. 106452. doi: [10.1016/j.jseaes.2024.106452](https://doi.org/10.1016/j.jseaes.2024.106452)
- Kim, J.I., Choi, S.H., Koh, G.W., Park, J.B., and Ryu, J.S., 2019, Petrogenesis and mantle source characteristics of volcanic rocks on Jeju Island, South Korea: *Lithos*, v. 326–327, p. 476–490. doi: [10.1016/j.lithos.2018.12.034](https://doi.org/10.1016/j.lithos.2018.12.034)
- Kim, K.H., Nagao, K., Sumino, H., Tanaka, T., Hayashi, T., Nakamura, T., and Lee, J.I., 2008, He–ar and Nd–sr isotopic compositions of late pleistocene felsic plutonic back arc basin rocks from Ulleungdo volcanic island, South Korea: Implications for the genesis of young plutonic rocks in a back arc basin: *Chemical Geology*, v. 253, p. 180–195. doi: [10.1016/j.chemgeo.2008.05.009](https://doi.org/10.1016/j.chemgeo.2008.05.009)
- Kim, Y.-W., Chang, S.-J., Witek, M., Ning, J., and Wen, J., 2021, S-velocity mantle structure of East Asia from teleseismic traveltimes tomography: Inferred mechanisms for the cenozoic intraplate volcanoes: *Journal of Geophysical Research: Solid Earth*, v. 126, p. e2020JB020345. doi: [10.1029/2020JB020345](https://doi.org/10.1029/2020JB020345)
- Lawrence, J.F., and Shearer, P.M., 2006, A global study of transition zone thickness using receiver functions: *Journal of Geophysical Research: Solid Earth*, v. 111, p. B06307. doi: [10.1029/2005JB003973](https://doi.org/10.1029/2005JB003973)
- Lee, S.H., Rhie, J., Park, Y., and Kim, K.H., 2014, Topography of the 410 and 660 km discontinuities beneath the Korean Peninsula and southwestern Japan using teleseismic receiver functions: *Journal of Geophysical Research: Solid Earth*, v. 119, p. 7245–7257. doi: [10.1002/2014JB011149](https://doi.org/10.1002/2014JB011149)
- Lee, W., Lee, H., Kim, D., Kim, J., Oh, J., Song, J.H., Kim, C.H., Park, C.H., and Stuart, F.M., 2021, Trace element and helium isotope geochemistry of the Cenozoic intraplate volcanism in the East Sea (Sea of Japan): Implications for lithosphere–asthenosphere interaction: *Lithos*, v. 388, p. 106075 doi: [10.1016/j.lithos.2021.106075](https://doi.org/10.1016/j.lithos.2021.106075)
- Lee, W., Lee, H., Kim, H., Song, J.H., Hong, J., Park, J., Jung, H., Lee, J., Takahata, N., Sano, Y., and Fischer, T.P., 2025, Water and gas geochemistry of springs in Ulleungdo volcano, South Korea: Implications for degassing of upper mantle-derived volatiles in northeast Asia: *Journal of Hydrology*, v. 647, p. 132286. doi: [10.1016/j.jhydrol.2024.132286](https://doi.org/10.1016/j.jhydrol.2024.132286)
- Li, J., Chen, Q.F., Vanacore, E., and Niu, F., 2008, Topography of the 660-km discontinuity beneath northeast China: Implications for a retrograde motion of the subducting Pacific slab: *Geophysical Research Letters*, v. 35, p. L01302. doi: [10.1029/2007GL031658](https://doi.org/10.1029/2007GL031658)
- Li, X., Sobolev, S.V., Kind, R., Yuan, X., and Estabrook, C., 2000, A detailed receiver function image of the upper mantle discontinuities in the Japan subduction zone: *Earth and Planetary Science Letters*, v. 183, p. 527–541. doi: [10.1016/S0012-821X\(00\)00294-6](https://doi.org/10.1016/S0012-821X(00)00294-6)
- Li, X., and Yuan, X., 2003, Receiver functions in northeast China—implications for slab penetration into the lower mantle in northwest Pacific subduction zone: *Earth and*



- Planetary Science Letters, v. 216, p. 679–691. doi: [10.1016/S0012-821X\(03\)00555-7](https://doi.org/10.1016/S0012-821X(03)00555-7)
- Ligorria, J.P., and Ammon, C.J., 1999, Iterative deconvolution and receiver-function estimation: *Bulletin of the Seismological Society of America*, v. 89, p. 1395–1400. doi: [10.1785/BSSA0890051395](https://doi.org/10.1785/BSSA0890051395)
- Litasov, K.D., Ohtani, E., Sano, A., Suzuki, A., and Funakoshi, K., 2005, Wet subduction versus cold subduction: *Geophysical Research Letters*, v. 32, p. L13312 doi:[10.1029/2005GL022921](https://doi.org/10.1029/2005GL022921).
- Liu, L., Gao, S.S., Liu, K.H., Griffin, W.L., Li, S., Tong, S., and Ning, J., 2022, Mantle dynamics of the north China craton: New insights from mantle transition zone imaging constrained by P-to-S receiver functions: *Geophysical Journal International*, v. 231, p. 629–637. doi: [10.1093/gji/ggac210](https://doi.org/10.1093/gji/ggac210)
- Liu, S.-A., Wu, T., Li, S., Wang, Z., and Liu, J., 2022, Contrasting fates of subducting carbon related to different oceanic slabs in East Asia: *Geochimica et Cosmochimica Acta*, v. 324, p. 156–173. doi: [10.1016/j.gca.2022.03.009](https://doi.org/10.1016/j.gca.2022.03.009)
- Liu, S., King, S.D., Long, M.D., Benoit, M.H., and Aragon, J.C., 2023, Receiver function analysis reveals lateral variations in temperature and water content in the mantle transition zone beneath eastern north America: *Geophysical Research Letters*, v. 50, p. e2022GL101965. doi: [10.1029/2022GL101965](https://doi.org/10.1029/2022GL101965)
- Liu, X., Zhao, D., Li, S., and Wei, W., 2017, Age of the subducting pacific slab beneath East Asia and its geodynamic implications: *Earth and Planetary Science Letters*, v. 464, p. 166–174. doi: [10.1016/j.epsl.2017.02.024](https://doi.org/10.1016/j.epsl.2017.02.024)
- Liu, Z., Niu, F., Chen, Y.J., Grand, S., Kawakatsu, H., Ning, J., Tanaka, S., Obayashi, M., and Ni, J., 2015, Receiver function images of the mantle transition zone beneath NE China: New constraints on intraplate volcanism, deep subduction and their potential link: *Earth and Planetary Science Letters*, v. 412, p. 101–111 doi:[10.1016/j.epsl.2014.12.019](https://doi.org/10.1016/j.epsl.2014.12.019).
- Liu, Z., Park, J., and Karato, S.I., 2016, Seismological detection of low-velocity anomalies surrounding the mantle transition zone in Japan subduction zone: *Geophysical Research Letters*, v. 43, p. 2480–2487 doi:[10.1002/2015GL067097](https://doi.org/10.1002/2015GL067097).
- Lu, C., Grand, S.P., Lai, H., and Garnero, E.J., 2019, TX2019slab: A new P and S tomography model incorporating subducting slabs: *Journal of Geophysical Research: Solid Earth*, v. 124, p. 11549–11567. doi: [10.1029/2019JB017448](https://doi.org/10.1029/2019JB017448)
- Miyazaki, K., and Nakajima, J., 2025, Flat 410 and 660 discontinuities beneath northeastern Japan: Implication for a sub-slab wet plume hypothesis: *Physics of the Earth and Planetary Interiors*, v. 361, p. 107316. doi: [10.1016/j.pepi.2025.107316](https://doi.org/10.1016/j.pepi.2025.107316)
- Moon, I., Lee, H., Kim, J., Oh, J., Seoung, D., Kim, C.H., Park, C.H., and Lee, I., 2020, Ti-magnetite crystallization in melt inclusions of trachytic rocks from the Dokdo and Ulleung islands, South Korea: Implications for hydrous and oxidized magmatism: Implications for Hydrous and Oxidized Magmatism: *Minerals*, v. 10, p. 644. doi: [10.3390/min10070644](https://doi.org/10.3390/min10070644)
- Muir, J.M., Zhang, F., and Brodholt, J.P., 2021, The effect of water on the post-spinel transition and evidence for extreme water contents at the bottom of the transition zone: *Earth and Planetary Science Letters*, v. 565, p. 116909. doi: [10.1016/j.epsl.2021.116909](https://doi.org/10.1016/j.epsl.2021.116909)
- Niu, F., Levander, A., Ham, S., and Obayashi, M., 2005, Mapping the subducting Pacific slab beneath southwest Japan with Hi-net receiver functions: *Earth and Planetary Science Letters*, v. 239, p. 9–17. doi: [10.1016/j.epsl.2005.08.009](https://doi.org/10.1016/j.epsl.2005.08.009)
- Obayashi, M., Yoshimitsu, J., and Fukao, Y., 2009, Tearing of stagnant slab: *Science*, v. 324, p. 1173–1175. doi: [10.1126/science.1172496](https://doi.org/10.1126/science.1172496)
- Obayashi, M., Yoshimitsu, J., Nolet, G., Fukao, Y., Shiobara, H., Sugioka, H., Miyamachi, H., and Gao, Y., 2013, Finite frequency whole mantle P wave tomography: Improvement of subducted slab images: *Geophysical Research Letters*, v. 40, p. 5652–5657. doi: [10.1002/2013GL057401](https://doi.org/10.1002/2013GL057401)
- Ramesh, D.S., Kawakatsu, H., Watada, S., and Yuan, X., 2005, Receiver function images of the central chugoku region in the Japanese islands using Hi-net data: *Earth, Planets and Space*, v. 57, p. 271–280. doi: [10.1186/BF03352563](https://doi.org/10.1186/BF03352563)
- Randall, G.E., 1994, Efficient calculation of complete differential seismograms for laterally homogeneous earth models: *Geophysical Journal International*, v. 118, p. 245–254. doi: [10.1111/j.1365-246X.1994.tb04687.x](https://doi.org/10.1111/j.1365-246X.1994.tb04687.x)
- Rawlinson, N., Fichtner, A., Sambridge, M., and Young, M.K., 2014, Seismic tomography and the assessment of uncertainty: *Advances in Geophysics*, v. 55, p. 1–76 doi:[10.1016/BS.AGPH.2014.08.001](https://doi.org/10.1016/BS.AGPH.2014.08.001).
- Schmerr, N., and Garnero, E.J., 2007, Upper mantle discontinuity topography from thermal and chemical heterogeneity: *Science*, v. 318, p. 623–626. doi: [10.1126/science.1145962](https://doi.org/10.1126/science.1145962)
- Shcheka, S.S., Wiedenbeck, M., Frost, D.J., and Keppler, H., 2006, Carbon solubility in mantle minerals: *Earth and Planetary Science Letters*, v. 245, p. 730–742. doi: [10.1016/j.epsl.2006.03.036](https://doi.org/10.1016/j.epsl.2006.03.036)
- Shin, Y.H., Choi, K.S., Koh, J.S., Yun, S.H., Nakamura, E., and Na, S. H., 2012, Lithospheric-folding-based understanding on the origin of the back-arc basaltic magmatism beneath Jeju volcanic island: *Tectonics*, v. 31, p. TC4005. doi: [10.1029/2011TC003092](https://doi.org/10.1029/2011TC003092)
- Simutè, S., Steptoe, H., Cobden, L., Gokhberg, A., and Fichtner, A., 2016, Full-waveform inversion of the Japanese islands region: *Journal of Geophysical Research: Solid Earth*, v. 121, p. 3722–3741. doi: [10.1002/2016JB012802](https://doi.org/10.1002/2016JB012802)
- Son, Y.O., Seo, M.S., and Kim, Y., 2022, Measurement of seismometer misorientation based on P-wave polarization: Application to permanent seismic network in South Korea: *Geosciences Journal*, v. 26, p. 235–247. doi: [10.1007/s12303-021-0031-5](https://doi.org/10.1007/s12303-021-0031-5)
- Song, J.H., Kim, S., and Rhee, J., 2020, Heterogeneous modification and reactivation of a craton margin beneath the Korean Peninsula from teleseismic travel time tomography: *Gondwana Research*, v. 81, p. 475–489. doi: [10.1016/j.gr.2019.11.016](https://doi.org/10.1016/j.gr.2019.11.016)
- Song, J.H., Kim, S., Rhee, J., Lee, S.H., Kim, Y., and Kang, T.S., 2018, Imaging of lithospheric structure beneath Jeju volcanic Island by teleseismic travelttime tomography: *Journal of Geophysical Research: Solid Earth*, v. 123, p. 6784–6801 doi:[10.1029/2018JB015979](https://doi.org/10.1029/2018JB015979).
- Sun, M., Gao, S.S., Liu, K.H., and Fu, X., 2020, Upper mantle and mantle transition zone thermal and water content anomalies beneath NE Asia: Constraints from receiver function imaging of the 410 and 660 km discontinuities: *Earth and Planetary Science Letters*, v. 532, p. 116040. doi: [10.1016/j.epsl.2019.116040](https://doi.org/10.1016/j.epsl.2019.116040)
- Sun, M., Yu, Y., Gao, S.S., and Liu, K.H., 2022, Stagnation and tearing of the subducting northwest Pacific slab: *Geology*, v. 50, p. 676–680. doi: [10.1130/G49862.1](https://doi.org/10.1130/G49862.1)

- Tao, K., Grand, S.P., and Niu, F., 2018, Seismic structure of the upper mantle beneath eastern Asia from full waveform seismic tomography: *Geochemistry, Geophysics, Geosystems*, v. 19, p. 2732–2763. doi: [10.1029/2018G007460](https://doi.org/10.1029/2018G007460)
- Tatsumi, Y., Shukuno, H., Yoshikawa, M., Chang, Q., Sato, K., and Lee, M.W., 2005, The petrology and geochemistry of volcanic rocks on Jeju Island: Plume magmatism along the Asian continental margin: *Journal of Petrology*, v. 46, p. 523–553. doi: [10.1093/petrology/egh087](https://doi.org/10.1093/petrology/egh087)
- Tauzin, B., Kim, S., and Kennett, B.L.N., 2017, Pervasive seismic low-velocity zones within stagnant plates in the mantle transition zone: Thermal or compositional origin?: *Earth and Planetary Science Letters*, v. 477, p. 1–13. doi: [10.1016/j.epsl.2017.08.006](https://doi.org/10.1016/j.epsl.2017.08.006)
- Tauzin, B., Waszek, L., Ballmer, M.D., Afonso, J.C., and Bodin, T., 2022, Basaltic reservoirs in the Earth's mantle transition zone: *Proceedings of the National Academy of Sciences*, v. 119, p. e2209399119. doi: [10.1073/pnas.2209399119](https://doi.org/10.1073/pnas.2209399119)
- Thomson, A.R., Walter, M.J., Kohn, S.C., and Brooker, R.A., 2016, Slab melting as a barrier to deep carbon subduction: *Nature*, v. 529, p. 76–79. doi: [10.1038/nature16174](https://doi.org/10.1038/nature16174)
- Tian, Y., Zhu, H., Zhao, D., Liu, C., Feng, X., Liu, T., and Ma, J., 2016, Mantle transition zone structure beneath the Changbai volcano: Insight into deep slab dehydration and hot upwelling near the 410 km discontinuity: *Journal of Geophysical Research: Solid Earth*, v. 121, p. 5794–5808. doi: [10.1002/2016JB012959](https://doi.org/10.1002/2016JB012959)
- Tibi, R., Wiens, D.A., Shiobara, H., Sugioka, H., and Yuan, X., 2007, Double seismic discontinuities at the base of the mantle transition zone near the Mariana slab: *Geophysical Research Letters*, v. 34, p. L16316. doi: [10.1029/2007GL030527](https://doi.org/10.1029/2007GL030527)
- Tonegawa, T., Hirahara, K., and Shibutani, T., 2005, Detailed structure of the upper mantle discontinuities around the Japan subduction zone imaged by receiver function analyses: *Earth, Planets and Space*, v. 57, p. 5–14. doi: [10.1186/BF03351801](https://doi.org/10.1186/BF03351801)
- Vacher, P., Mocquet, A., and Sotin, C., 1998, Computation of seismic profiles from mineral physics: The importance of the non-olivine components for explaining the 660 km depth discontinuity: *Physics of the Earth and Planetary Interiors*, v. 106, p. 275–298 doi:[10.1016/S0031-9201\(98\)00076-4](https://doi.org/10.1016/S0031-9201(98)00076-4).
- Wang, B., and Niu, F., 2010, A broad 660 km discontinuity beneath northeast China revealed by dense regional seismic networks in China: *Journal of Geophysical Research: Solid Earth*, v. 115, p. B06308. doi: [10.1029/2009JB006608](https://doi.org/10.1029/2009JB006608)
- Wang, L., and He, X., 2020, Sharpness of the paired 660-km discontinuity beneath the Izu-Bonin area: *Earth and Planetary Physics*, v. 4, p. 627–638 doi:[10.26464/epp2020067](https://doi.org/10.26464/epp2020067).
- Waszek, L., Anandawansha, R., Sexton, J., and Tauzin, B., 2024, Thermochemistry of the mantle transition zone beneath the western pacific: *Geophysical Research Letters*, v. 51, p. e2024GL110852. doi: [10.1029/2024GL110852](https://doi.org/10.1029/2024GL110852)
- Wei, W., and Zhao, D., 2020, Intraplate volcanism and mantle dynamics of mainland China: New constraints from shear-wave tomography: *Journal of Asian Earth Sciences*, v. 188, p. 104103. doi: [10.1016/j.jseaes.2019.104103](https://doi.org/10.1016/j.jseaes.2019.104103)
- Xi, Z., Chen, M., Wei, S.S., Li, J., Zhou, T., Wang, B., and Kim, Y., 2024, EARA2024: A new radially anisotropic seismic velocity model for the crust and upper mantle beneath East Asia and northwestern pacific subduction zones: *Geophysical Journal International*, v. 239, p. 914–935 doi:[10.1093/gji/ggae302](https://doi.org/10.1093/gji/ggae302).
- Xu, W., Lithgow-Bertelloni, C., Stixrude, L., and Ritsema, J., 2008, The effect of bulk composition and temperature on mantle seismic structure: *Earth and Planetary Science Letters*, v. 275, p. 70–79 doi:[10.1016/j.epsl.2008.08.012](https://doi.org/10.1016/j.epsl.2008.08.012).
- Yang, J., and Faccenda, M., 2020, Intraplate volcanism originating from upwelling hydrous mantle transition zone: *Nature*, v. 579, p. 88–91. doi: [10.1038/s41586-020-2045-y](https://doi.org/10.1038/s41586-020-2045-y)
- Yu, C., Goes, S., Day, E.A., and van der Hilst, R.D., 2023, Seismic evidence for global basalt accumulation in the mantle transition zone: *Science Advances*, v. 9, p. eadg0095. doi: [10.1126/sciadv.adg0095](https://doi.org/10.1126/sciadv.adg0095)
- Zang, S.X., Zhou, Y.Z., Ning, J.Y., and Wei, R.Q., 2006, Multiple discontinuities near 660 km beneath tonga area: *Geophysical Research Letters*, v. 33, p. L20312. doi: [10.1029/2006GL027262](https://doi.org/10.1029/2006GL027262)
- Zhang, R., Gao, Z., Wu, Q., Xie, Z., and Zhang, G., 2016, Seismic images of the mantle transition zone beneath northeast China and the Sino-Korean craton from P-wave receiver functions: *Tectonophysics*, v. 675, p. 159–167 doi:[10.1016/j.tecto.2016.03.002](https://doi.org/10.1016/j.tecto.2016.03.002).
- Zhao, D., 2021, Seismic imaging of northwest Pacific and East Asia: New insight into volcanism, seismogenesis and geodynamics: *Earth-Science Reviews*, v. 214, p. 103507. doi: [10.1016/j.earscirev.2021.103507](https://doi.org/10.1016/j.earscirev.2021.103507)
- Zhao, D., Tian, Y., Lei, J., Liu, L., and Zheng, S., 2009, Seismic image and origin of the Changbai intraplate volcano in East Asia: Role of big mantle wedge above the stagnant pacific slab: *Physics of the Earth and Planetary Interiors*, v. 173, p. 197–206. doi: [10.1016/j.pepi.2008.11.009](https://doi.org/10.1016/j.pepi.2008.11.009)
- Zhao, D., Toyokuni, G., and Kim, Y., 2025, Changbai intraplate volcanism and big mantle wedge: *Physics of the Earth and Planetary Interiors*, v. 367, p. 107425. doi: [10.1016/j.pepi.2025.107425](https://doi.org/10.1016/j.pepi.2025.107425)